



The newly developed Multi-ensemble Biomass-burning Emissions Inventory (MBEI): Characterizing and unraveling spatiotemporal uncertainty in global biomass burning emissions

Xinlu Liu^{1,2}, Zhongyi Sun^{2*}, Chong Shi¹, Peng Wang³, Tangzhe Nie⁴, Qingnan Chu⁵, Huazhe Shang¹, Lu Sun⁶, Dabin Ji¹, Meng Guo⁷, Kunpeng Yi⁸, Zhenghong Tan⁹, Lan Wu², Xinchun Lu^{1,3}, Shuai Yin^{1*}

¹State Key Laboratory of Remote Sensing and Digital Earth, Aerospace Information Research Institute, Chinese Academy of Sciences, Beijing 100101, China

²College of Ecology and Environment, Hainan University, Haikou 570228, China

³Department of Atmospheric and Oceanic Sciences, Fudan University, Shanghai, 200438, China

⁴School of Water Conservancy and Electric Power, Heilongjiang University, Harbin 150006, China

⁵Centro de Biotecnología y Genómica de Planta (UPM-INIA). Universidad Politécnica de Madrid, Campus de Montegancedo, Madrid, Spain

⁶School of Human Settlements and Civil Engineering, Xi'an Jiaotong University, Shaanxi Province, 710049, China

⁷School of Geographical Sciences, Northeast Normal University, Changchun 130024, China

⁸State Key Laboratory of Urban and Regional Ecology, Research Center for Eco-Environmental Sciences, Chinese Academy of Sciences, Beijing 100085, China

⁹School of Ecology and Environmental Science, Yunnan University, Kunming 650500, China

Correspondence: Shuai Yin (vinshuai@aircas.ac.cn) and Zhongyi Sun (gis.rs@hainanu.edu.cn)



Abstract. Against the backdrop of global climate change, the spatiotemporal patterns of biomass burning are undergoing significant changes. However, large discrepancies among different emission inventories hinder a consensus on the true magnitude and long-term trends of global emissions. This study constructs a framework for estimating biomass burning emissions by integrating bottom-up and top-down approaches with various combinations of multi-source data inputs, resulting in the development of the Multi-ensemble Biomass-burning Emissions Inventory (MBEI). Leveraging this framework, we develop the MBEI global emission dataset covering the period 2003–2023, which comprises eight sub-inventories and provides emission estimates for 11 representative greenhouse gases, aerosols, and atmospheric pollutants, including CO₂, PM_{2.5}, BC, NO₂, and others. A unique feature of MBEI is its ability to quantify the uncertainty in biomass burning emission estimates across various spatial scales, achieved by calculating the average emissions and their Max-Min band at a 0.1° grid scale from these sub-inventories. The analysis reveals that the global annual CO₂ emissions from biomass burning are approximately 7304 7304 (4400–9657) Tg, with the maximum value being more than double the minimum. Furthermore, the uncertainty in global biomass burning emissions exhibits significant spatial heterogeneity: in low-emission regions such as Australia and the Middle East, the ratio of maximum to minimum emission estimates can reach 6.0–7.0 fold, whereas in traditional hotspots like Africa and South America, this ratio is lower, around 1.9 fold. In terms of temporal trends, global emissions showed a decreasing trend from 2003 to 2013, primarily driven by a reduction in burning activities in tropical regions. This trend, however, reversed to an increase from 2013 to 2023, with the primary drivers being intensified burning in northern high-latitude regions and the frequent occurrence of extreme events. Finally, a comparison with existing inventories confirms the reliability of the MBEI dataset. At both global and regional scales, the average of our inventory is centrally positioned among other inventory estimates in most years, offering a more robust central estimate for assessing biomass burning emission intensity during extreme event years. Moreover, its maximum-minimum range encompasses the estimates of other inventories across most regions and time periods. This capability to characterize uncertainty enables the integration of the new datasets MBEI into analytical frameworks, such as atmospheric chemistry models and exposure risk assessments, thereby enhancing the reliability of global biomass burning dynamics analyses and the robustness of the conclusions. The Multi-ensemble Biomass-burning Emissions Inventory (MBEI) dataset is publicly available at <https://doi.org/10.5281/zenodo.17128279> (Liu and Yin, 2023).



66 1 Introduction

67 Biomass burning, encompassing forest fires, grassland fires, and the burning of agricultural residues, is
 68 a key disturbance in terrestrial ecosystems. It profoundly influences local and global ecological processes
 69 and climate systems by releasing large quantities of greenhouse gases (GHGs) and aerosol particles
 70 (Bowman et al., 2009; Letu et al., 2023; Pellegrini et al., 2018; Shi et al., 2025; Yin, 2021). Accelerating
 71 climate change is driving significant shifts in the spatiotemporal patterns of global biomass burning,
 72 affecting its frequency, intensity, and duration. Observational data indicate that the incidence of extreme
 73 biomass burning events has increased 2.2-fold in the last two decades (Cunningham et al., 2024; Wang
 74 et al., 2023), and climate models project that high-risk areas for global biomass burning will expand by
 75 nearly one-third by the end of the 21st century (Senande-Rivera et al., 2022). Notably, while the burned
 76 area is shrinking in some traditional high-frequency burning regions (e.g., tropical rainforests) (Andela
 77 et al., 2017; Zheng et al., 2021), the fire-prone season is substantially extending. In regions such as
 78 southeastern Australia, eastern Siberia, and eastern North America, the length of fire weather season has
 79 increased by 27%–94%, significantly prolonging the period during which ecosystems are exposed to fire
 80 risk (Jones et al., 2022).

81 The increase of biomass burning frequency is raising atmospheric concentrations of GHGs, thereby
 82 exerting a strong perturbation on Earth's biospheric processes (Andreae, 2019; Andreae and Merlet, 2001;
 83 Yin et al., 2025). Between 1997 and 2016, global carbon emissions from biomass burning averaged 2.2
 84 Pg C per year, equivalent to approximately 6% of global fossil fuel CO₂ emissions in 2014 (Friedlingstein
 85 et al., 2025; Liu et al., 2024; van der Werf et al., 2017). This increase in GHGs intensifies global warming,
 86 creating a feedback loop that is projected to elevate the risk of extreme fire weather by at least 50% in
 87 key regions such as western North America, equatorial Africa, Southeast Asia, and Australia by 2080
 88 (Touma et al., 2021). Furthermore, particulate matter (e.g., black carbon, brown carbon, and organic
 89 carbon) emitted from biomass burning poses a serious threat to human health (Reid et al., 2005; Zhang
 90 et al., 2020). A meta-analysis of 81 studies (1980–2020) by Karanasiou et al (2021). showed that exposure
 91 to PM_{2.5} and PM₁₀ from biomass burning is significantly associated with all-cause mortality,
 92 corresponding to a 1.31% (95% CI: 0.71–1.71) and 1.92% (95% CI: 1.19–5.03) increase for every 10 µg
 93 m⁻³ rise in PM₁₀ and PM_{2.5}. These effect sizes exceed typical estimates for all-source ambient particulate
 94 matter, indicating that biomass burning PM may pose greater health risks than general ambient PM. From



1990 to 2019, PM_{2.5}-related excess mortality in equatorial Asia increased threefold, with approximately 317 thousand of these deaths attributed to high-intensity biomass burning from Indonesian peatlands (Yin, 2023).

Establishing high-precision emission inventories is crucial for assessing the impacts of biomass burning on the global atmospheric environment and public health (Bray et al., 2021; Filonchyk et al., 2024; Ramanathan and Carmichael, 2008). Trace gases and aerosols released by biomass burning not only affect global climate but also alter regional atmospheric chemistry via transboundary transport (Andreae, 2019). Atmospheric Chemistry Transport Models used for air quality forecasting and source apportionment, rely on emission inventories with high spatiotemporal resolution and reliability. Such data are crucial for accurately resolving pollutant transport and transformation pathways, as well as for quantifying their contributions to pollution (Matthias et al., 2018; Wang et al., 2014). Currently, the construction of global and regional biomass burning emission inventories primarily relies on two established estimation pathways, the bottom-up and top-down approach. The bottom-up approach typically estimates emissions based on satellite-derived burned area (e.g., MODIS MCD64A1) combined with fuel load, combustion completeness, and emission factors (van der Werf et al., 2017; Wiedinmyer et al., 2023). The typical inventories of this approach include the Global Fire Emissions Database (GFED) and the Fire INventory from NCAR (FINN) (Giglio et al., 2006). In contrast, the alternative top-down approach estimates emissions based on Fire Radiative Power (FRP) retrieved from satellites in thermal infrared bands. This method utilizes the relationship between the time-integrated FRP, known as Fire Radiative Energy (FRE), and the total dry matter consumed, a relationship often calibrated using field observations (Ichoku and Ellison, 2014; Wooster et al., 2005). It estimates emissions by fitting the combustion curve of dry matter consumption derived from satellite-retrieved FRP (Santoro, 2018). The typical inventories include the Global Fire Assimilation System (GFAS) and the Quick Fire Emissions Dataset (QFED) (Andela et al., 2015; Giglio et al., 2020).

Although these two methods provide clear theoretical frameworks, their practical implementation varies among researchers in their choice of data sources, parameters, and algorithmic details, leading to significant discrepancies in the resulting inventories (Hoelzemann et al., 2004; Ichoku and Kaufman, 2005; Ito and Penner, 2004; Zhang et al., 2014). Consequently, estimates of total emissions for the same region or period can differ considerably (N'Datchoh et al., 2025; Pereira et al., 2016; Shi and Matsunaga, 2017; Whitburn et al., 2015). This discrepancy poses a key challenge in the field, as it not only directly



125 impacts the accuracy of atmospheric chemistry simulations and climate effect assessments (Liu et al.,
 126 2020; Longo et al., 2010; Stroppiana et al., 2010; Williams et al., 2012) but also leads to a lack of clear
 127 consensus on the true magnitude and long-term trends of global biomass burning emissions.

128 A growing body of evidence suggests that under the dual threats of climate change and human activities,
 129 the spatial distribution of global biomass burning is undergoing significant shifts. Fire activity is
 130 weakening in some traditional tropical hotspots (e.g., African savannas) while intensifying in high-
 131 latitude boreal forests (Tyukavina et al., 2022; van Wees et al., 2021; Yin et al., 2020b; Zheng et al., 2021,
 132 2023). These complex and opposing regional trends obscure the long-term trajectory of global total
 133 emissions. In this context, the limitation of emission inventories, which provide only a single estimate,
 134 becomes more prominent. A single value cannot capture the extent to which observed regional trends
 135 reflect genuine physical processes versus mere algorithmic artifacts of a particular inventory. Therefore,
 136 accurately assessing the current state of biomass burning emissions requires not only improving the
 137 precision of inventories but also developing new methods to systematically quantify their uncertainty.

138 To address this challenge, we constructed the Multi-ensemble Biomass-burning Emissions Inventory
 139 (MBEI), a global biomass burning emission dataset for 2003–2023, by integrating mainstream top-down
 140 and bottom-up algorithms. This ensemble approach incorporates two fire-detection products and four
 141 sets of key input variables, resulting in eight distinct sub-inventories that quantify emissions for 11 key
 142 species (e.g., CO₂, PM_{2.5}, BC, and NO₂). By analyzing the mean and the maximum-minimum range
 143 (hereafter referred to as the "Max-Min band") of these eight sub-inventories, our study provides a new
 144 quantitative estimate of global biomass burning emissions over the past 21 years and, crucially, reveals
 145 their uncertainty across various spatial scales. It offers quantitative evidence to better interpret the shifts
 146 in global biomass burning patterns. The advantages of this new inventory allow data users (such as
 147 atmospheric chemistry modelers and climate assessment experts) to directly incorporate the variability
 148 of emission estimates into their analytical frameworks, thereby providing critical data support for
 149 dissecting complex global biomass burning dynamics and enhancing the robustness of their assessment
 150 results.

151

152



153 **2 Materials and Methods**

154 **2.1 Datasets**

155 The MBEI integrates two established methodologies: a bottom-up approach based on burned area and a
156 top-down approach based on FRP (Vermote et al., 2009; Wiedinmyer et al., 2006). Active fire detections
157 were sourced from the MODIS Near-Real-Time product (MCD14DL). To assess uncertainty stemming
158 from detection confidence, we created two parallel processing streams using fire pixels from both Aqua
159 and Terra satellites (2003–2023): one including all detected fires, and another restricted to fires with
160 medium-to-high confidence (>30%). In addition, we introduced combination in key input variables: the
161 bottom-up algorithm was driven by two alternative aboveground biomass (AGB) datasets (Biomass_cci
162 and GlobBiomass), while the top-down algorithm utilized two different biome maps (8-class and 30-
163 class) to define emission coefficients. For consistency, all input datasets were resampled to a common
164 0.1° spatial resolution and monthly temporal resolution. A comprehensive list of the datasets used in this
165 study is provided in Table 1.

166

167

168

169

170

171

172

173

174

175

176

177

178

179

180

181



182

Table 1. Datasets used in this study.

Data types	Name	Temporal Coverage	Spatial Resolution	Temporal Resolution	Reference
Active Fire Data	Aqua MCD14DL	2003-2023	1 km × 1 km	daily	(NASA VIIRS Land Science Team, 2021)
	Terra MCD14DL	2003-2023	1 km × 1 km	daily	
Burning Efficiency (BE) & Emission Factor (EF) Data	Land Cover Type MCD12Q1.061	2003-2023	500 m × 500 m	yearly	(Friedl and Sulla-Menashe, 2022)
	EF Classification Source Data GFED	\	0.25° × 0.25°	\	(van der Werf et al., 2006)
	EF Coefficients	\	\	\	(van der Werf et al., 2017)
	BE Coefficients	\	\	\	(Shi et al., 2015)
	GlobBiomass	2010	25 m × 25 m	\	(Santoro, 2018)
AGB Data	Biomass_cci	2010/2015-2021	100 m × 100 m	yearly	(Santoro and Cartus, 2024)
Conversion Factor (CR) Data	30-class CR map	\	0.1° × 0.1°	\	(Kaiser et al., 2023)
	8-class CR map	\	0.1° × 0.1°	\	(Kaiser et al., 2012)
Ancillary & Validation Data	Annual Gross/Net Primary Production (NPP) MYD17A3HGF v061	2003-2023	500 m × 500 m	yearly	(Running and Zhao, 2021)
	Global Fire Emissions Database 5 (GFED 5)	2003-2022	0.25° × 0.25°	daily	(Binte Shahid et al., 2024; Vernooij et al., 2023; Wiggins et al., 2021)
	Fire INventory from NCAR 2.5 (FINN 2.5) MODIS	2002-2022	0.1° × 0.1°	daily	(Wiedinmyer et al., 2023)
	Global Fire Assimilation System 1.2 (GFAS 1.2)	2003-2022	0.1° × 0.1°	daily	(Kaiser et al., 2012)
	Quick Fire Emissions Dataset 3.1 (QFED3.1)	2003-2022	0.1° × 0.1°	daily	(Koster et al., 2015)

Note: The 8-class biome map is derived from the 30-class biome map. See Fig. S1 for its spatial distribution.

185



186 **2.1.1 Active fire detection and fire radiative power**

187 The sourced active fire data were obtained from the MODIS Near-Real-Time active fire product
 188 (MCD14DL C6.1), provided by NASA's Fire Information for Resource Management System (FIRMS).
 189 This product provides fire detections from both the Terra and Aqua satellites based on the
 190 MOD14/MYD14 thermal anomalies algorithm (Giglio et al., 2006). Each active fire detection represents
 191 the center of a 1-km pixel flagged as containing one or more fires.
 192 For the period 2003–2023, we extracted daily fire locations, detection confidence, and FRP values. These
 193 1-km daily data were then aggregated into monthly 0.1° grids, which form the primary input for both our
 194 top-down and bottom-up frameworks.

195 **2.1.2 Burning efficiency and emission factor**

196 To assign region- and vegetation-specific BE and EF, we first utilized the annual 500-m MODIS Land
 197 Cover Type product (MCD12Q1 C6.1), adopting its International Geosphere-Biosphere Programme
 198 (IGBP) classification scheme. We then assigned a BE value to each of the 17 IGBP classes using
 199 coefficients derived from Mieville et al. (2010) and Shi et al. (2015), with the specific values detailed in
 200 Table S3.
 201 Emission factors were assigned by intersecting the MCD12Q1 land cover map with the 14 continental-
 202 scale regions defined by GFED (van der Werf et al., 2017). This process yielded a unique EF for each
 203 landcover region combination, allowing us to estimate emissions for 11 key atmospheric emission
 204 species as detailed in Table S4.

205 **2.1.3 Aboveground biomass**

206 To quantify available fuel load for the bottom-up framework and assess related uncertainties, we
 207 employed two independent global AGB datasets. The GlobBiomass provides a global AGB map at 25-m
 208 spatial resolution for the baseline year 2010, generated by synergistically fusing multi-source data,
 209 including observations from spaceborne Synthetic Aperture Radar (SAR), Light Detection and Ranging
 210 (LiDAR), and optical remote sensing, together with forest inventory data (Santoro, 2018). Biomass_cci,
 211 provided by the European Space Agency Climate Change Initiative (ESA CCI) project, contains global
 212 AGB maps at 100-m resolution for multiple years (2010, 2017, 2018, and annually for 2019–2021)
 213 (Mariani et al., 2016).



214 **2.1.4 Conversion factor**

215 In the top-down method, satellite-derived FRE, which is the temporal integral of FRP, is converted into
 216 the mass of combusted dry matter. This conversion is performed using a biome-specific conversion factor
 217 (kg Dry Matter MJ⁻¹). To assess the uncertainty associated with this parameter, we implemented two
 218 distinct sets of conversion factors: one based on the 8 major biomes used in the GFAS (Kaiser et al.,
 219 2012), and another based on a more detailed 30-class biome map. The spatial distributions and respective
 220 CR values for these two schemes are detailed in Figs. S1–S2 and Tables S1–S2.

221 **2.1.5 Ancillary and validation data**

222 To derive a dynamic annual AGB time series for 2003–2022 from otherwise static AGB maps, we used
 223 the MODIS annual Net Primary Production product MYD17A3HGF v061, which provides global NPP
 224 at 500 m spatial resolution. We leveraged the empirically supported linear relationship between NPP and
 225 AGB to temporally extrapolate the baseline AGB maps and generate annual AGB maps, with the detailed
 226 procedure and parameterization described in Section 2.2.1.

227 To evaluate the performance and robustness of the new inventory, we conducted a comprehensive
 228 intercomparison with four widely used global emission products that span both bottom-up and FRP
 229 methodologies. For the bottom-up approach, GFED 5.0 serves as a key benchmark, as its reliance on the
 230 Carnegie–Ames–Stanford Approach (CASA) biogeochemical model for fuel load estimation allows for
 231 a critical assessment of how a model-driven workflow differs from our use of direct remotely sensed
 232 AGB. To specifically isolate the influence of parameter choices (e.g., emission factors and burning
 233 efficiency), we included FINN 2.5 in our analysis. Because it is built upon the same MODIS active fire
 234 and land cover inputs, a comparison with FINN 2.5 provides a controlled setting to evaluate the impact
 235 of our system's unique parameterization. For the top-down FRP-based approach, GFAS 1.2 provides a
 236 reference for evaluating the plausibility of the combustion-rate coefficient schemes tested in this study,
 237 as it converts satellite-observed FRP to dry matter combusted in a manner consistent with our framework.
 238 Finally, we incorporated QFED 3.1, which represents an optimized evolution of GFAS applying more
 239 advanced correction and gap-filling procedures, to examine how alternative imputation strategies for
 240 missing FRP retrievals affect the spatiotemporal completeness of the final emission estimates.



2.2 The framework for the MBEI

We constructed the MBEI, which integrates bottom-up and top-down algorithms with multiple input datasets, yielding an ensemble of eight distinct sub-inventories (see Table 2 for the naming conventions). This framework leverages the strengths of different estimation pathways while systematically assessing uncertainties arising from methodological choices and input data. Using this framework, we compute mean emissions across global regions, thereby improving the reliability of the estimates. Crucially, in contrast to traditional single-estimate inventories, we also report grid-scale maxima and minima from the ensemble to explicitly quantify the range of emission uncertainties. The overall workflow is illustrated in Fig. 1.

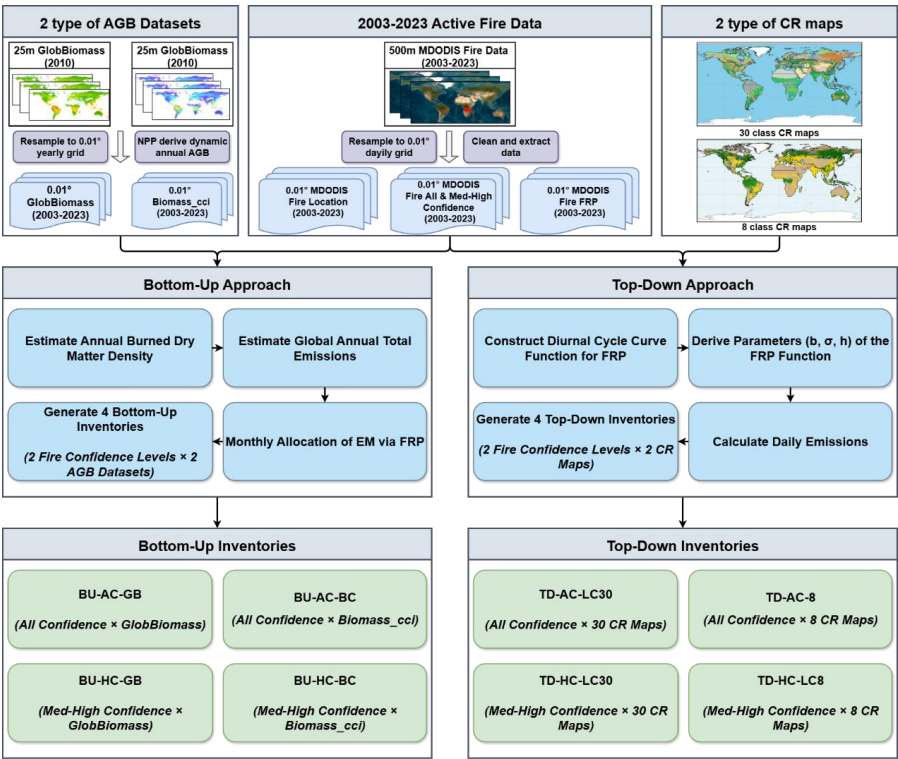


Figure 1. Framework for the construction of MBEI.



Table 2. The detail of the eight biomass burning emission sub-inventories.

4 Bottom-Up Inventories			4 Top-Down Inventories		
Name	Confidence Level	Datasets	Name	Confidence Level	Datasets
BU-AC-GB	All Confidence	GlobBiomass	TD-AC-LC30	All Confidence	30-class CR map
BU-AC-BC	All Confidence	Biomass_cci	TD-AC-LC8	All Confidence	8-class CR map
BU-HC-GB	Medium-to-High confidence	GlobBiomass	TD-HC-LC30	Medium-to-High confidence	30-class CR map
BU-HC-BC	Medium-to-High confidence	Biomass_cci	TD-HC-LC8	Medium-to-High confidence	8-class CR map

2.2.1 Bottom-up emission estimation

This study employs a bottom-up method, combining multi-source remote sensing data to construct four global monthly biomass burning emission inventories for 2003–2023. The core computational workflow involves four key steps: (1) constructing a dynamic annual AGB dataset based on interannual variations in NPP; (2) modeling the total burned dry matter density (BD) under multiple fire events within a year; (3) estimating total annual emissions (EM) by burned area (BA), BD and EF; (4) downscaling annual emissions to a monthly resolution using the monthly distribution of FRP.

To overcome the limitation of using a static AGB benchmark map that ignores interannual variability, we constructed a dynamic annual AGB dataset. Based on the ecological assumption of a stable proportional relationship between AGB and NPP (Raich et al., 2006; Whittaker and Likens, 1972), we used the relative interannual changes in the MODIS annual NPP product to extrapolate the baseline AGB. The AGB for a target year (m) in a specific pixel (p) is calculated as:

$$AGB_{(m,p)} = AGB_{(a,p)} \times \frac{NPP_{(m,p)}}{NPP_{(a,p)}} \quad (1)$$

where $AGB_{(m,p)}$ is the AGB in year m at pixel p ($Mg\ ha^{-1}$); $AGB_{(a,p)}$ is the baseline AGB at pixel p (mean of 2003–2023, $Mg\ ha^{-1}$); $NPP_{(m,p)}$ is the NPP in year m at pixel p ($kg\ C\ m^{-2}\ yr^{-1}$); and $NPP_{(a,p)}$ is the baseline mean NPP at pixel p ($kg\ C\ m^{-2}\ yr^{-1}$).

After obtaining annual AGB, we estimated the annual BD per unit area. Considering that a pixel may experience multiple fires in a year, we used the following model to simulate the sequential consumption of AGB by fire and accumulate the total annual burned amount:



$$BD_{(m,p)} = \sum_{j=1}^I \{AGB_{(m,p)} \times (1 - BE_c)^{j-1} \times BE_c\} \quad (2)$$

where $BD_{(m,p)}$ is the total burned dry matter density in year m at pixel p (kg m^{-2}); I is the fire frequency in year m at pixel p (derived from active fire data); j represents the j -th fire event of the year; $AGB_{(m,p)}$ is the initial AGB at the beginning of the year (kg m^{-2}); and BE_c is the dimensionless burning efficiency for the land cover type c of pixel p .

The total annual emissions of each pollutant are estimated based on the method proposed by Seiler and Crutzen (1980):

$$EM_{(m,p)} = BA_{(m,p)} \times BD_{(m,p)} \times EF \quad (3)$$

where $EM_{(m,p)}$ is the annual emission of a specific pollutant in year m at pixel p (g); $BA_{(m,p)}$ is the total annual burned area in year m at pixel p (m^2), obtained by multiplying the annual MODIS active fire location mask by the pixel's geographic area to ensure that the burned location is consistent with fire detections; $BD_{(m,p)}$ is the annual burned dry matter density (kg m^{-2}) calculated from Eq. (2); and EF is the emission factor for the specific pollutant (g kg^{-1}).

To obtain a monthly-resolution emission inventory, we used satellite-observed FRP as a proxy for fire activity intensity to distribute the annual emissions $EM_{(m,p)}$ into each month (t):

$$EM_{(m,p,t)} = EM_{(m,p)} \times \frac{FRP_{(m,p,t)}}{\sum_{t=1}^{12} FRP_{(m,p,t)}} \quad (4)$$

where $EM_{(m,p,t)}$ is the pollutant emission in month t of year m at pixel p (g); and $FRP_{(m,p,t)}$ is the monthly cumulative FRP in month t of year m at pixel p (MJ s^{-1}).

2.2.2 Top-down emission estimation

Our top-down emission estimation is based on the FRP approach, which uses satellite-observed thermal radiation to quantify biomass burning. The entire computational framework revolves around FRE, with the final pollutant emissions calculated as:

$$EM_{(p)} = FRE_{(p)} \times CR_{(r)} \times EF \quad (5)$$

where $EM_{(p)}$ is the daily emission at pixel p (g); $FRE_{(p)}$ is the daily cumulative FRE at pixel p (MJ); $CR_{(r)}$ is the conversion factor for the biome r where pixel p is located ($\text{kg Dry Matter MJ}^{-1}$); and EF is the emission factor for the specific pollutant (g kg^{-1}).

However, polar-orbiting satellites like MODIS provide only limited observations per day, making it impossible to obtain daily cumulative FRE by simple integration of instantaneous FRP. To overcome this,



we reconstruct the FRP diurnal cycle by fitting a Gaussian function, following the methodology of Vermote et al. (2009). We assume that the diurnal variation of FRP for a single biomass burning event can be represented by a Gaussian function:

$$FRE_{(p)} = \int_0^{24} FRP(t)_{(p)} dt = \int_0^{24} FRP_{peak(p)} \left(b + e^{-\frac{(t-h)^2}{2\sigma^2}} \right) dt \quad (6)$$

where $FRP(t)_{(p)}$ is the instantaneous FRP at local time t for pixel p ; $FRP_{peak(p)}$ is the peak FRP of the fire event at pixel p ($MJ s^{-1}$); h is the local time of peak FRP hours; σ is the standard deviation of the Gaussian function, characterizing energy release concentration of the fire; and b is a background term reflecting residual or background radiation during non-active burning periods. The Gaussian parameters b , σ , and h are empirically derived for each biome from the long-term mean FRP ratio between Terra and Aqua observations using the relationships (henceforth $\frac{\overline{FRP}_{Terra}}{\overline{FRP}_{Aqua}}$):

$$b = 0.86 \times \left(\frac{\overline{FRP}_{Terra}}{\overline{FRP}_{Aqua}} \right)^2 - 0.52 \times \frac{\overline{FRP}_{Terra}}{\overline{FRP}_{Aqua}} + 0.08 \quad (7)$$

$$\sigma = 3.89 \times \frac{\overline{FRP}_{Terra}}{\overline{FRP}_{Aqua}} + 1.03 \quad (8)$$

$$h = -1.23 \times \frac{\overline{FRP}_{Terra}}{\overline{FRP}_{Aqua}} + 14.57 \quad (9)$$

where \overline{FRP}_{Terra} and \overline{FRP}_{Aqua} are the long-term mean FRP values for the respective sensors within that biome ($MJ s^{-1}$).

The final FRP_{peak} is determined by selecting either the daily peak FRP from the Aqua satellite (henceforth FRP_{Aqua_peak}) or the daily peak FRP from the Terra satellite after correction with Eq. (12) (henceforth FRP_{Terra_corr}):

$$FRP_{Aqua_peak(p)} = \frac{FRP_{Aqua(p)}}{\left(b + e^{-\frac{(1.5-h)^2}{2\sigma^2}} \right) + \left(b + e^{-\frac{(13.5-h)^2}{2\sigma^2}} \right)} \quad (10)$$

$$FRP_{Terra_peak(p)} = \frac{FRP_{Terra_corr(p)}}{\left(b + e^{-\frac{(1.5-h)^2}{2\sigma^2}} \right) + \left(b + e^{-\frac{(13.5-h)^2}{2\sigma^2}} \right)} \quad (11)$$

$$FRP_{Terra_corr(p)} = FRP_{Terra(p)} \times \frac{\overline{FRP}_{Terra}}{\overline{FRP}_{Aqua}} \quad (12)$$

where $FRP_{Terra_corr(p)}$ is the corrected Terra FRP at pixel p ($MJ s^{-1}$), FRP_{peak} was calculated from Aqua satellite data using Eq. (10), following the approach of Vermote et al. (2009). Additionally, FRP values from the Terra satellite were adjusted using Eq. (12). This adjustment utilized long-term FRP ratios for



different biomes to normalize the morning Terra observations to the afternoon measurement time of the Aqua satellite.

Independent daily FRE estimates were then calculated using the original Aqua observations (FRP_{Aqua} $_{peak(p)}$) and the corrected Terra observations ($FRE_{Terra\ peak(p)}$) in Eq. (6) at pixel p ($MJ\ s^{-1}$). The final daily FRE is the average of these two estimates:

$$FRE_{(p)} = \frac{FRE_{Aqua(p)} + FRE_{Terra(p)}}{2} \quad (13)$$

Through these steps, we obtained the final daily FRE data. We then used Eq. (5) to calculate emissions and aggregated them to a monthly scale, ultimately producing four independent top-down emission inventories.

2.3 Trend analysis

Long-term trends in biomass burning emissions (2003–2022) were quantified using the Theil-Sen median trend estimator, with statistical significance assessed by the Mann-Kendall (MK) test (Mann, 1945; Sen, 1968). This non-parametric approach is particularly suitable for geophysical time series like emission data, as it is robust to outliers and does not assume a normal distribution.

The Theil-Sen estimator calculates the median of the slopes between all pairs of data points in the time series, making it robust to outliers (e.g., emission peaks from extreme fire years) and providing a stable estimate of the long-term trend. The slope is calculated as:

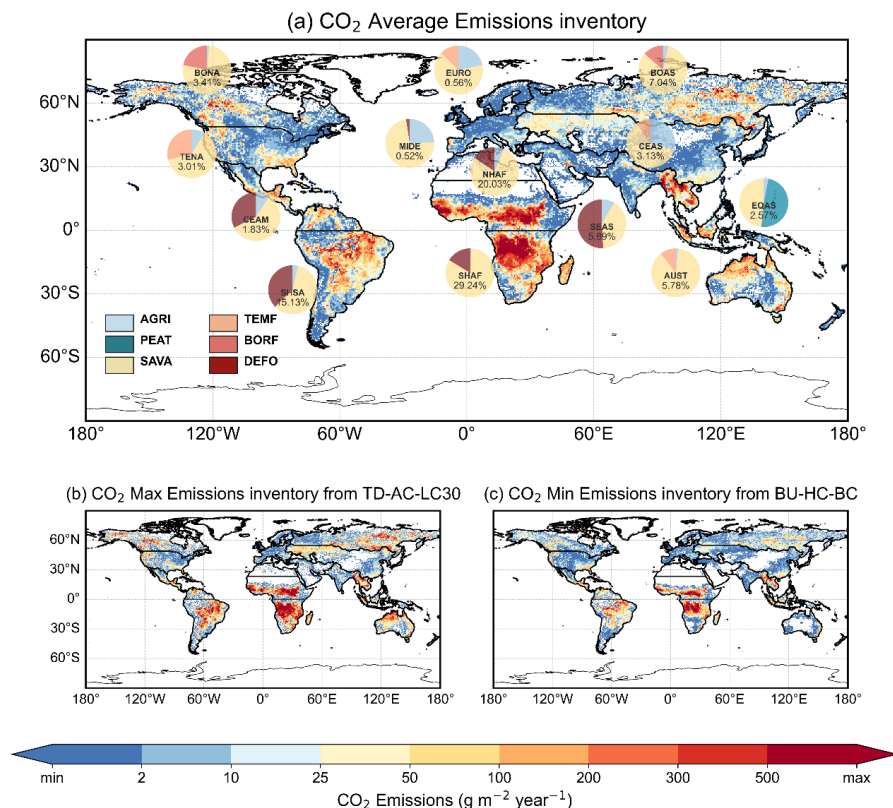
$$\text{slope} = \text{median} \frac{x_j - x_i}{j - i} \quad (1 \leq i < j \leq n) \quad (14)$$

where slope is the estimated trend, x_i and x_j are the data values at time points i and j , and n is the length of the time series.



334 **3 Results**

335 **3.1 Spatial patterns and uncertainty of global biomass burning emissions**



336

337 **Figure 2. Spatial patterns and regional composition of global biomass burning CO₂ emissions (mean of 2003–**
338 **2023). (a) Spatial distribution of the annual mean CO₂ emission flux estimated from the mean of the eight**
339 **inventories in this study. The embedded pie charts show the emission composition for 14 major regions, where:**
340 **1) the number in the pie chart indicates the percentage of that region's emissions relative to the global total;**
341 **and 2) the sectors of the pie chart represent the proportional contribution of six major fire types to the region's**
342 **total emissions. (b) and (c) show the spatial emission patterns corresponding to the inventory with the highest**
343 **global total annual emissions (TD-AC-LC30) and the lowest global total annual emissions (BU-HC-BC)**
344 **among the eight inventories over the entire study period, respectively.**

345

346 CO₂ is a principal greenhouse gas and the most widely studied species in biomass-burning inventories;
347 accordingly, Sections 3.1–3.4 focus on CO₂, and results for other species are provided in the
348 Supplementary Information. For 2003 to 2023, the framework-mean global annual emissions for all
349 species are summarized in Table 3 and Table S5. The framework-mean CO₂ emission is 7303.63 Tg yr⁻¹,



350 and the associated uncertainty, quantified as the range of annual means across the eight sub-inventories
 351 in the ensemble, spans 4400.08 to 9656.89 Tg yr⁻¹.

352 Fig. 2 shows the highly heterogeneous spatial pattern of mean annual CO₂ emission fluxes (the spatial
 353 patterns for other major pollutants are presented in Fig. S6). Global emission activities are largely
 354 concentrated in tropical and subtropical regions, characterized by high emission fluxes (> 300 g m⁻² yr⁻¹).
 355 Within these areas, the most intense emission hotspots (> 500 g m⁻² yr⁻¹) are clearly identified over
 356 the Congo Basin, surrounding savannas, and parts of Southern Africa. This high spatial concentration of
 357 intense burning directly translates to Africa's dominant role in the global emission budget. Based on
 358 regional statistics (Global 14 regions defined in Fig. S3), Southern Hemisphere South Africa (SHAF)
 359 and Northern Hemisphere South Africa (NHAF) collectively contribute 49.2% of global CO₂ emissions
 360 (29.2% and 20.0%, respectively). Furthermore, Southern Hemisphere South America (SHSA, 15.1%),
 361 Boreal Asia (BOAS, 7.0%), and Southeast Asia (SEAS, 5.9%) also stand out as major source regions for
 362 global biomass burning.

363 The dominant types of biomass burning vary substantially by region (see Fig. S4 for the classification of
 364 fire types), leading to distinct emission profiles (see Fig. S5 for the composition of fire types in each
 365 region). In the top three emitting regions (SHAF, NHAF, and SHSA), which collectively account for
 366 nearly two-thirds (64.4%) of global CO₂ emissions, burning is driven primarily by savanna fires (SAVA)
 367 and deforestation fires (DEFO). The contribution of different fire types varies significantly among these
 368 top regions (see Fig. 2a for detailed emission values). In SHAF, the largest source, SAVA are
 369 overwhelmingly dominant, accounting for 83% of its CO₂ emissions. A similar pattern occurs in NHAF,
 370 where SAVA contributes 78% of emissions, although agricultural waste burning (AGRI) also plays a
 371 notable role (6%). In contrast, the emissions in SHSA are more evenly split between SAVA (59%) and
 372 DEFO fires (37%). In the high-latitude regions of BOAS and Boreal North America (BONA), fires in
 373 boreal forests (BORF) are a characteristic emission source, contributing 14% and 22% of regional CO₂
 374 emissions, respectively. Notably, our analysis identifies fires classified as SAVA as the largest contributor
 375 in both regions (83% in BOAS and 77% in BONA). It is critical to note that SAVA in this context refers
 376 to the burning of extensive grasslands and shrublands located within the boreal climate zone, as defined
 377 by our underlying land cover dataset, rather than tropical savannas. This highlights that non-forest fires
 378 are the dominant source of emissions even in these high-latitude zones.



379 The emission composition of Equatorial Asia (EQAS) is unique. Although its total emissions are
 380 relatively low, it is the only region dominated by peatland fires (PEAT), with PEAT emissions
 381 contributing as much as 91.34 Tg yr⁻¹ of CO₂ (48.4% of the regional total). This uniqueness stems from
 382 its specific fire regime: vast areas of organic-rich peatlands become highly flammable after being drained
 383 and converted to agricultural land (e.g., oil palm plantations). Such fires often manifest as long-duration,
 384 hard-to-extinguish subsurface smoldering, leading to extremely high carbon emission intensities and
 385 making EQAS a unique and closely watched case in global biomass burning research.

386 The spatial heterogeneity of this uncertainty is illustrated in Figs. 2b and 2c, which map the highest and
 387 lowest emission estimates across the ensemble. Globally, the uncertainty is substantial, with the
 388 maximum estimate of annual CO₂ emissions being 2.2 times higher than the minimum estimate across
 389 the MBEI sub-inventories.

390 Importantly, high biomass burning emission uncertainty is not found in traditional biomass burning
 391 hotspots. Instead, some of the highest uncertainties are found in regions with lower overall emissions.
 392 Specifically, Australia and New Zealand (AUST) and the Middle East (MIDE) exhibit the greatest
 393 uncertainty, with maximum-to-minimum (max/min) emission ratios reaching 7.18 and 6.40, respectively.
 394 In AUST, this extreme uncertainty is linked to its fire regime dominated by highly intermittent and
 395 catastrophic megafires (e.g., the 2019–2020 events), which pose significant challenges to consistent
 396 estimation across different algorithms. In MIDE, which contributes only 0.52% to the global total, the
 397 high uncertainty stems from small, scattered AGRI and SAVA. These weak fire signals are near the lower
 398 limit of satellite detection capabilities, a fact confirmed by the large discrepancy observed when
 399 comparing estimates derived from 'all confidence' versus 'high and medium confidence' active fire data.

400 In contrast, the major tropical burning regions show much lower relative uncertainty, despite their
 401 massive contribution to global emissions. The African (SHAF, NHAF) and South American (SHSA)
 402 hotspots have max/min ratios consistently below 2.0. This greater consensus among methods is
 403 attributable to the nature of their fires: large-scale, intense, and seasonally predictable SAVA that are
 404 robustly captured by various estimation approaches. Meanwhile, temperate and high-latitude regions
 405 such as Central Asia (CEAS), BONA, and Europe (EURO) show intermediate levels of uncertainty, with
 406 max/min ratios between 3.5 and 4.0.

407 In summary, this analysis reveals a critical divergence between the spatial patterns of emission
 408 magnitudes and their estimation uncertainties. While emission hotspots are concentrated in tropical



regions dominated by regular SAVA and DEFO, the highest uncertainties occur in areas characterized by either highly intermittent megafires (e.g., AUST) or weak, scattered burning (e.g., MIDE), posing distinct challenges to current estimation methods.

Table 3. Total annual CO₂ emissions (Maximum, Minimum, and Average, unit: Tg) for 2003–2023.

Year	Max	Min	Avg	Year	Max	Min	Avg
2003	10882.90	4487.65	7673.68	2014	9258.62	4489.87	7265.29
2004	10842.08	4271.50	7522.16	2015	9688.74	5035.46	7701.46
2005	10391.58	4350.62	7328.15	2016	8476.61	4059.68	6789.30
2006	9663.37	4160.83	7077.83	2017	9250.64	4436.15	7042.77
2007	11063.35	4641.22	7751.48	2018	8727.34	4160.93	6911.22
2008	9725.05	4030.68	6925.95	2019	9747.60	4971.22	7657.46
2009	8661.02	3930.36	6669.83	2020	9295.62	4375.98	7249.50
2010	10253.23	4748.50	7554.59	2021	10696.69	4767.44	7705.11
2011	9653.73	4119.74	7205.26	2022	7289.55	3348.45	6442.83
2012	10537.30	4721.32	7895.63	2023	10527.88	5206.72	8506.96
2013	8161.82	4087.36	6489.87	Mean	9656.89	4400.08	7303.16



3.2 Seasonality of biomass burning emissions

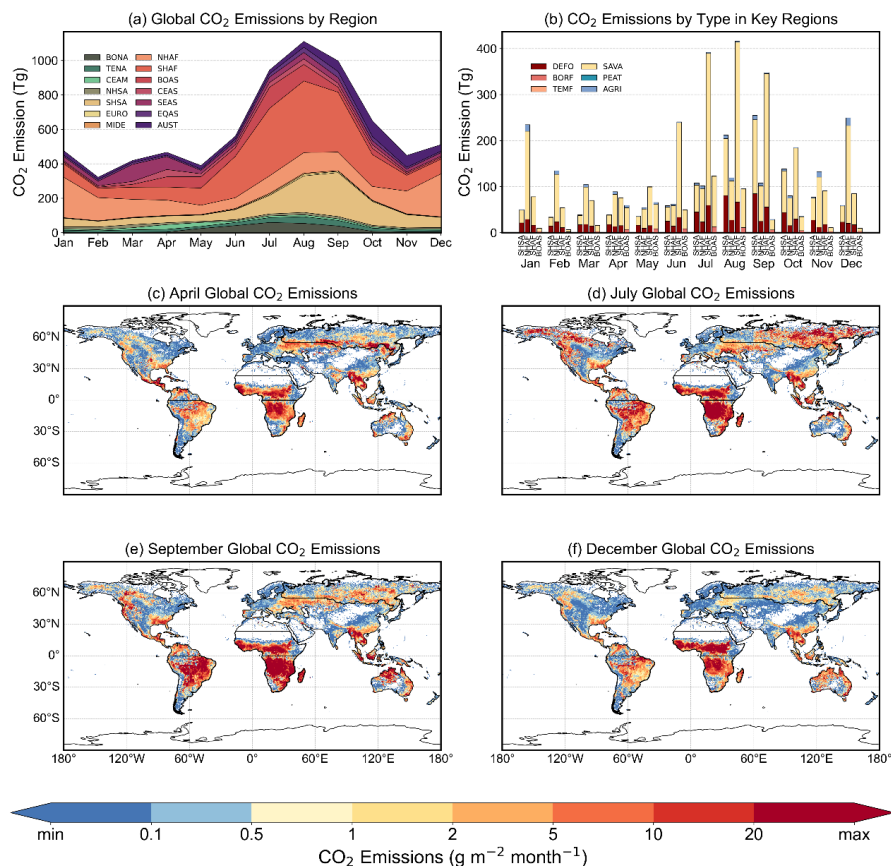


Figure 3. Seasonal cycle and spatial dynamics of global biomass burning CO₂ emissions (mean of 2003–2023).
(a) Global monthly emissions partitioned by source region. (b) Monthly emissions for the four primary contributing regions, showing the composition by fire type. (c–f) Spatial distribution of mean monthly emission flux during key seasonal phases: April, July, September, and December.

The MBEI 2003–2023 CO₂ emission inventory reveals a distinct bimodal seasonal cycle (Fig. 3a). Global emissions reach a minimum in February and then climb to a primary peak in the Northern Hemisphere's late summer (August–September). This global pattern results from the combined effect of staggered fire seasons in key regions. Four regions in particular (SHAF, NHAF, SHSA, and BOAS) drive this cycle, collectively accounting for over 71% of total annual emissions (Fig. 3b). For a detailed view of the emission sources, Fig. S7 shows the monthly composition of CO₂ emissions by the six fire types for each of the 14 global regions during 2003–2023.



429 The annual cycle begins its ascent after the global minimum in February, initially driven by fire activity
430 in the Northern Hemisphere. Persistent dry-season burning in NHAF transitions into an intensifying fire
431 season across Eurasia. By April, the focus of burning activity clearly shifts northward, with emissions
432 surging in regions like BOAS, while the major Southern Hemisphere burning regions (SHAF and SHSA)
433 remain in a period of low activity (Fig. 3c).
434 From May onwards, global emissions accelerate rapidly, driven by the increasing overlap of fire seasons
435 in both hemispheres. While boreal fires in regions like BOAS reach their annual peak in July, the
436 dominant driver of this global surge is the explosive onset of the fire season in SHAF. Concurrently,
437 burning intensifies in SHSA, and this synergistic effect pushes global emissions towards their annual
438 maximum (Fig. 3d).
439 The global emission peak in August and September is dominated by the Southern Hemisphere, as fire
440 activity wanes in the major Northern Hemisphere regions. During this period, burning in SHSA reaches
441 its annual zenith, fueled by a combination of DEFO and SAVA. Although past its own peak, SHAF
442 remains the single largest regional contributor to global emissions (Fig. 3e).
443 Beginning in October, the onset of the rainy season in the Southern Hemisphere rapidly suppresses fire
444 activity there, causing a sharp decline in global emissions. This marks a decisive shift in the global
445 burning pattern. The focus of activity returns entirely to NHAF, which enters its primary fire season that
446 lasts through the subsequent winter (Fig. 3f). This distinct hemispheric seesaw effect completes the
447 annual cycle. Fig. S8 present the spatial distribution patterns of monthly CO₂ emissions from global
448 biomass burning during the period 2003–2023.



3.3 Interannual variability and long-term trends

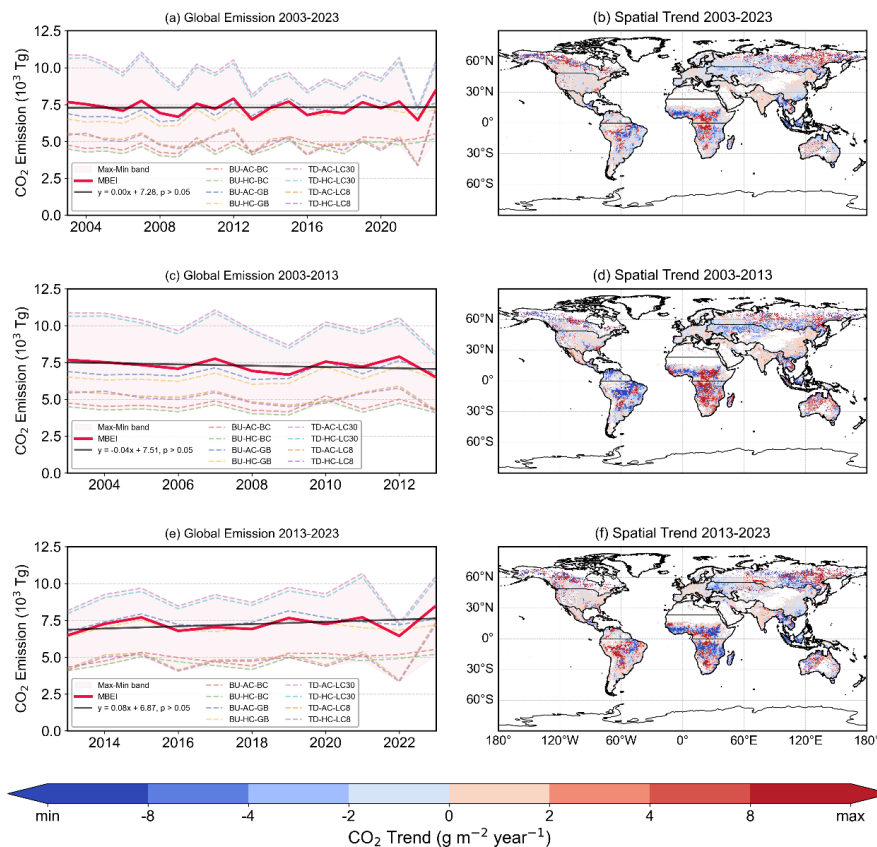


Figure 4. Temporal and spatial trends of global biomass burning CO₂ emissions from 2003 to 2023. (a, c, e) Interannual variation of total emissions and (b, d, f) trends in emission flux for three periods: 2003–2023, 2003–2013, and 2013–2023.

Over the 2003–2023 study period, global biomass burning CO₂ emissions are characterized not by a significant long-term trend but by pronounced interannual variability. Specifically, the time series of global annual CO₂ emissions, derived from the MBEI, which integrates eight sub-inventories, shows no statistically significant long-term trend ($p > 0.05$; Fig. 4a). This pattern of high interannual variability, coupled with a lack of a significant long-term trend, is also observed for other major emitted species (Fig. S9). This strong interannual variability is a well-documented feature of global fire activity, primarily linked to climate anomalies such as the El Niño-Southern Oscillation (ENSO) (Chen et al., 2017; Mariani et al., 2016; Li et al., 2023). Our time-series analysis confirms this link: emission peaks (e.g., 2010, 2015,



2019) consistently coincide with major El Niño events that trigger widespread drought, while emission troughs (e.g., 2009, 2022) align with wetter La Niña conditions. The sharp contrast between the low emissions during the 2022 La Niña and the subsequent spike during the 2023 El Niño starkly illustrates the powerful influence of the ENSO cycle on global fire activity.

Alongside these climate-driven variations, the MBEI is characterized by a broad uncertainty range, stemming from differences in algorithm structures and input data. The spread between MBEI estimates (the Max-Min band in Figs. 4a, c, e) is considerable, with the difference between the highest and lowest annual totals exceeding 2600 Tg in some years (e.g., 2004, 2022). This divergence arises from methodological differences, particularly between top-down (FRP-based) and bottom-up (burned area-based) approaches in areas like fire detection and combustion parameterization. Critically, however, despite the large spread in absolute emission values, the MBEI sub-inventories show strong agreement on the relative interannual patterns, consistently identifying the same peak and trough years.

This apparent global stability masks significant and opposing regional trends, producing a highly heterogeneous spatial pattern of change (Fig. 4b). Over the full 21-year period, statistically significant trends were concentrated in Asia. BOAS exhibited a strong and significant increasing trend in emission flux at a rate of $15.71 \text{ g m}^{-2} \text{ yr}^{-1}$ ($p < 0.01$). In contrast, CEAS and SEAS showed significant decreasing trends of $-1.72 \text{ g m}^{-2} \text{ yr}^{-1}$ ($p < 0.01$) and $-2.08 \text{ g m}^{-2} \text{ yr}^{-1}$ ($p < 0.05$), respectively. Fig. 4b suggests decreases in equatorial Africa and central-southern South America, and increases in BONA, these trends were not statistically significant when aggregated over the entire 14 GFED regions for the 2003–2023 period. This highlights an offsetting pattern, where declining emissions in some regions are partially balanced by increases elsewhere, contributing to the lack of a significant global trend.

A decadal comparison between 2003–2013 and 2013–2023 reveals substantial evolution in these spatial patterns, indicating a major shift in the global distribution of biomass burning emissions (Figs. 4d, f). During the first decade (2003–2013), a slight but statistically non-significant global decrease ($p > 0.05$; Fig. 4c) masked a profound spatial redistribution of fire activity. The dominant feature was a significant increase in fire emissions in SHAF, which saw an upward trend of $4.41 \text{ g m}^{-2} \text{ yr}^{-1}$ ($p < 0.05$). By contrast, South America experienced significant decreases, particularly in NHSA where emissions declined at a rate of $-4.97 \text{ g m}^{-2} \text{ yr}^{-1}$ ($p < 0.05$). Simultaneously, a strong decreasing trend was observed in CEAS, with a rate of $-2.96 \text{ g m}^{-2} \text{ yr}^{-1}$ ($p < 0.05$). Boreal regions and Southeast Asia showed no statistically significant regional trends during this period (Fig. 4d).



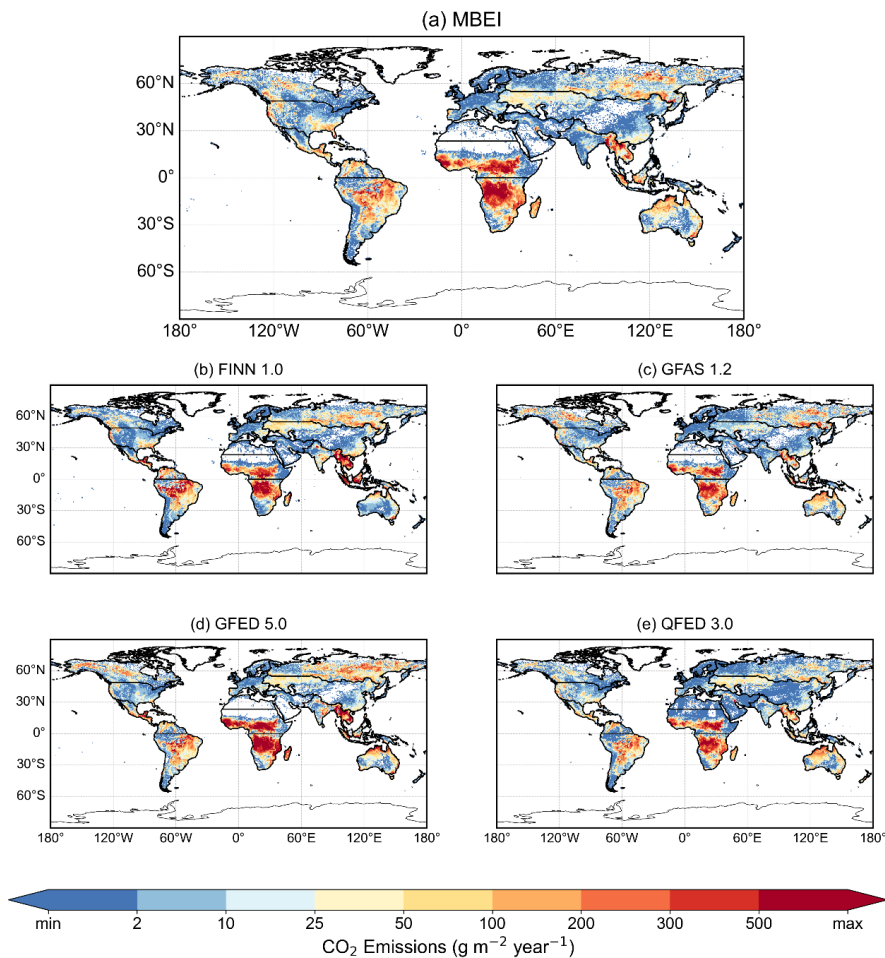
493 In the subsequent decade (2013–2023), this pattern shifted markedly. Although the global emission
 494 trajectory did not exhibit a statistically significant linear trend ($p > 0.05$), it transitioned from a slight
 495 decline to an overall increase (Fig. 4e), signaling a clear decadal change in biomass burning dynamics.
 496 This shift is more appropriately characterized as a structural transformation rather than a linear
 497 progression, driven by a marked increase in both the frequency and intensity of extreme emission years
 498 (e.g., 2015, 2019, 2023). The 2015–2016 ENSO cycle exemplifies this mechanism, as the super El Niño
 499 event in 2015 induced catastrophic PEAT in Indonesia (EQAS) and elevated global emissions to a record
 500 peak, which was subsequently followed by a pronounced decline in 2016 with the onset of a strong La
 501 Niña (Whitburn et al., 2016; Yin et al., 2020a). The 2023 fire season was even more pronounced, as an
 502 unprecedented wildfire season in boreal Canada (BONA) coincided with a developing El Niño, jointly
 503 driving global annual emissions to the highest level in our 21-year record (Jain et al., 2024; Luo et al.,
 504 2025).

505 Spatially, this decadal shift is characterized by a reversal of trends in Africa and South America (Fig. 4f).
 506 Africa, which previously showed increasing trends in the south, now exhibited a pronounced and
 507 significant decrease in NHAF, with emissions declining at $-5.14 \text{ g m}^{-2} \text{ yr}^{-1}$ ($p < 0.05$). In a direct reversal
 508 of the previous decade, SHSA showed a strong and significant increase of $8.01 \text{ g m}^{-2} \text{ yr}^{-1}$ ($p < 0.01$).
 509 Notably, despite the visually striking increases in BONA and northern Eurasia driven by the extreme fire
 510 years mentioned previously, the linear trends for these aggregated regions over the 2013–2023 period
 511 were not statistically significant, suggesting that the changes were dominated by episodic events rather
 512 than a consistent year-over-year increase.

513 In summary, beneath the overall stable trend of global biomass burning emissions over the past 21 years,
 514 there lies a key decadal shift, from a declining phase dominated by weakening fire activity in the tropics
 515 (2003–2013) to an increasing phase driven by intensifying fire activity in high-latitude regions and parts
 516 of the Southern Hemisphere (2013–2023).



517 3.4 Inter-comparison with other inventories



518
519 **Figure 5. Comparison of multi-year mean spatial patterns of global CO₂ emissions estimated by different**
520 **biomass burning inventories (2003–2022). (a) The mean of the eight inventories constructed in this study. (b)**
521 **Fire INventory from NCAR version 2.5 (FINN 2.5), (c) Global Fire Assimilation System version 1.2 (GFAS**
522 **1.2), (d) Global Fire Emissions Database version 5.0 (GFED 5.0), and (e) Quick Fire Emissions Dataset version**
523 **3.1 (QFED 3.1).**

524

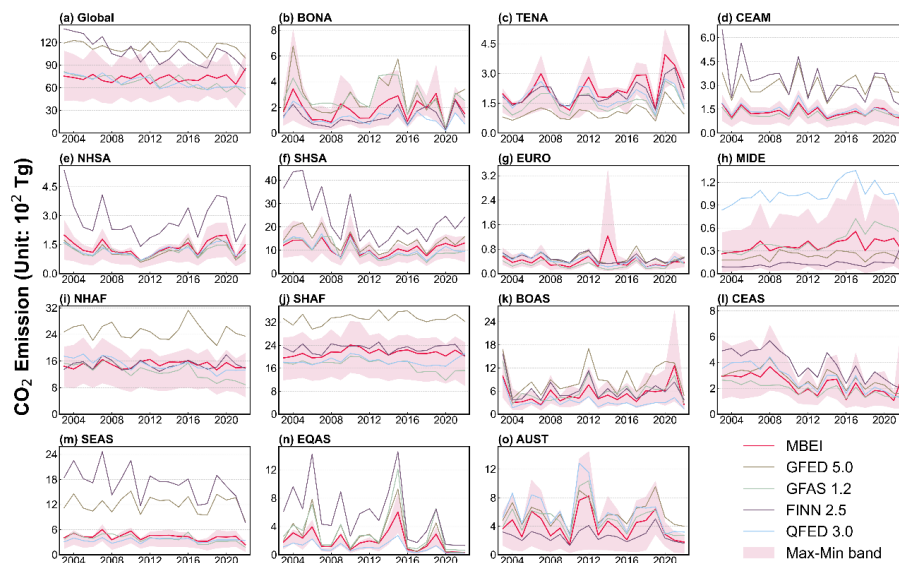


Figure 6. Time series of interannual variability in biomass burning CO₂ emissions from different inventories at global and regional scales (2003–2022). (a) Total annual global CO₂ emissions from this study's inventory and four other inventories. (b) to (o) Total annual CO₂ emissions from this study's inventory and four other inventories across 14 regions.

A comparison of biomass burning CO₂ emissions reveals broad spatial agreement across all inventories (including the MBEI from this study, FINN 2.5, GFAS 1.2, GFED 5.0, and QFED 3.1) (Fig. 5). Furthermore, the emission magnitudes from these inventories are largely consistent, with no significant discrepancies. In addition, comparative analyses are performed for three emission species, namely SO₂, PM_{2.5} and BC and the results are presented in Figs. S10–S15 in the Supplementary Material. These species represent different components and combustion phases of biomass burning. SO₂ reflects the combustion of naturally occurring sulfur-containing organic matter and inorganic sulfides in biomass, PM_{2.5} represents the overall intensity of total particulate matter emissions, and BC indicates incomplete combustion during the high-temperature flaming phase. Similar to CO₂, the spatial patterns for these species are largely consistent across inventories. While the products capture similar interannual variability, their estimates of emission magnitudes reveal substantial inter-inventory uncertainty (results show in Figs. S10–S15). All products successfully identify the primary global fire hotspots, including those in Africa (SHAF, NHAF), South America (SHSA), Southeast Asia (SEAS), and the northern boreal forests (BONA, BOAS).



545 However, significant discrepancies exist in both emission magnitude and spatial detail among various
 546 inventories (Fig. 6). The uncertainty range (Max–Min band) of the MBEI generally encompasses the
 547 estimates from all reference products across most regions, suggesting that it effectively captures the
 548 structural uncertainty among inventories. Moreover, the mean estimate of the MBEI typically resides
 549 near the center of the various inventories. With respect to magnitude and trend, our inventory exhibits
 550 the closest alignment with GFAS. GFED consistently provides the highest global estimates, while FINN
 551 ranks second and in some regions even exceeds GFED, whereas QFED remains generally lower. Despite
 552 these differences in magnitude, all inventories demonstrate strong consistency in interannual variability,
 553 successfully capturing major global fire years (e.g., 2010, 2015, 2019).

554 A regional analysis highlights significant divergences among emission inventories, particularly in the
 555 high-emission tropics where the MBEI's uncertainty band is often substantial. In the African savannas
 556 (NHAF, SHAF), the MBEI mean estimate is consistently lower than GFED 5.0, often residing in the
 557 lower half of the inter-inventory range (Figs. 6i, j). For instance, in SHAF, GFED 5.0 estimates are
 558 frequently approximately 10 Tg yr⁻¹ higher than the MBEI mean, while our estimate aligns closely with
 559 GFAS 1.2 and QFED 3.0. Conversely, in regions with significant DEFO and AGRI fires like SHSA and
 560 SEAS, FINN 2.5 estimates consistently occupy the upper portion of the inter-inventory range. In these
 561 areas, the MBEI mean is again more conservative, and our Max-Min band effectively captures the cluster
 562 of lower estimates from GFED, GFAS, and QFED (Figs. 6f, m).

563 In contrast, inter-inventory agreement is generally higher in low- to moderate-emission regions at mid-
 564 to high latitudes, where the MBEI mean closely tracks the multi-inventory average (e.g., Temperate North
 565 American (TENA) and EURO; Figs. 6c, 6g). However, this consistency breaks down in boreal forests
 566 during years with episodic, large-scale fires. In these instances, the value of the Max-Min band becomes
 567 particularly evident. During the extreme BONA fire year of 2004, estimates spanned a wide range from
 568 FINN 2.5 (2.2 Tg) to GFED 5.0 (6.7 Tg). Critically, our own Max-Min band for that year expanded
 569 dramatically (from 1.0 to 8.0 Tg), explicitly quantifying the immense challenge and uncertainty in
 570 capturing such events. A similar expansion of our uncertainty band is observed in BOAS during its severe
 571 2021 fire season, where our maximum estimate reached 26.8 Tg, encompassing the high values from
 572 other inventories.

573 Regions dominated by specific fuel types, such as the peatlands of EQAS, reveal fundamental
 574 methodological differences that are well-framed by our uncertainty analysis. While all inventories



575 captured the 2015 El Niño-driven fire peak, the estimated magnitude varied by more than five-fold, from
 576 QFED 3.0 (2.7 Tg) to FINN 2.5 (14.6 Tg) (Fig. 6n). The MBEI mean estimate (6.0 Tg) and its associated
 577 uncertainty band (3.2–8.6 Tg) are positioned centrally among these estimates, with its upper bound
 578 approaching the GFED 5.0 value (9.3 Tg) while excluding the extreme high and low outliers. This
 579 indicates that, under substantial uncertainty in quantifying PEAT emissions, the MBEI delineates a
 580 comprehensive Max–Min band and provides a stable central mean estimate within it.

581 In summary, our comparison demonstrates that while existing inventories agree on broad spatiotemporal
 582 patterns, significant quantitative disagreements persist, particularly in tropical regions and during
 583 extreme fire events. Against this backdrop, the MBEI provides a new, synthesized central estimate and a
 584 robust uncertainty range (Min–Max band). Its central estimate is consistent with the ensemble median,
 585 and its uncertainty bounds effectively encompass the spread across different inventories. This central
 586 estimate and a quantified uncertainty range not only offers a reliable measure of biomass burning
 587 emissions but also serves as a diagnostic tool, highlighting the specific regions (e.g., African savannas,
 588 Southeast Asian peatlands) and conditions (e.g., extreme boreal fires) that drive the largest inter-
 589 inventory discrepancies, thereby providing a clear basis for future inventory refinement.

590 **4 Discussion**

591 **4.1 Advancement and uncertainty assessment**

592 This study introduces the MBEI, a systematic emission estimation framework built upon a framework of
 593 eight sub-inventories, integrating both bottom-up and top-down approaches with various combinations
 594 of key input data. The emission range of the MBEI provides a direct measure of structural uncertainty,
 595 allowing modelers to assess the sensitivity of their simulations to inventory choice (high-end vs. low-
 596 end estimates). This addresses a long-standing challenge in climate and atmospheric chemistry modeling,
 597 where discrepancies among emission inventories are a recognized major source of the simulation
 598 uncertainty (Pan et al., 2020; Su et al., 2023). The MBEI framework systematically quantifies this
 599 uncertainty, revealing two key findings. First, the uncertainty is substantial in magnitude, with the
 600 maximum global annual CO₂ estimate across the sub-inventories being 2.2 times the minimum. Second,
 601 and perhaps more importantly, the uncertainty exhibits significant spatial heterogeneity, with the highest



relative uncertainty not coinciding with traditional emission hotspots, but instead found in regions with lower emissions, such as AUST and MIDE.

This divergence is strongly linked to how regional land cover and fire regime characteristics amplify the sensitivity of different estimation methodologies. For instance, in AUST, the fire regime is dominated by event-driven, extremely high-intensity megafires. These events pose significant challenges for both FRP-based algorithms, which can be prone to saturation, and burned area-based methods, which struggle to accurately map such intense and rapidly spreading fires. Conversely, in the MIDE, the high uncertainty arises from weak, small-scale, and scattered AGRI or SAVA. These fires are often near the detection limits of satellite sensors, causing emission estimates to be highly sensitive to the chosen active fire detection confidence thresholds. In stark contrast, African savannas, despite their high emission fluxes, show lower relative uncertainty. Their widespread and seasonally predictable fires are robustly captured by both top-down and bottom-up approaches, leading to greater convergence among the different methods. This finding implies that future efforts to refine emission inventories should extend beyond traditional hotspots to better understand and parameterize the distinct combustion processes in these atypical fire regimes.

The MBEI's 21-year analysis also uncovers a critical shift in the long-term dynamics of global emissions. Despite a stable trend overall, we identify a clear decadal transition: from a slight decline dominated by weakening tropical fires (2003–2013) to a rising phase driven by intensifying boreal fires and more frequent extreme events (2013–2023). This dynamic, characterized by a decline in tropical fire activity and an increase in boreal fire activity, synthesizes seemingly disparate observations, such as the global decrease in burned area (Andela et al., 2017) and the lengthening of fire seasons in high-latitude regions (Jones et al., 2022), into a coherent narrative at the emission level. Particularly in the second decade, climate-driven extreme events, such as the 2015 Indonesian peat fires, the 2019–2020 Australian megafires, and the 2023 Canadian wildfires, significantly reshaped the global emission record. This underscores the growing influence of climate change on global biomass burning emissions, a shift with profound implications for the global carbon cycle and its associated climate feedbacks.

4.2 Perspective of the MBEI framework

A key feature of the MBEI framework is its flexibility and scalable design, allowing for future improvements as new data and methods become available. The accuracy of the inventory is intrinsically



linked to its inputs, and we identify clear pathways for enhancement in both the bottom-up and top-down approaches. For the bottom-up path, fuel load remains the dominant source of uncertainty. This uncertainty is amplified by the combustion structures unique to each biome, an issue that the static nature of current AGB products struggles to resolve. For example, in boreal forests, the thick litter and duff layers on the forest floor can sustain long-duration smoldering, making total fuel consumption highly sensitive to burn depth, which is notoriously difficult to estimate. Similarly, in peatlands, the immense carbon stock in subterranean organic soil means that emission estimates are critically dependent on the depth of burn, a highly variable parameter. In tropical forests, while total biomass is high, fires are often patchy, and a large fraction of the coarse woody debris may not combust in a single event. In contrast, savanna and grassland fuels, being well-ventilated and predominantly composed of fine, dry herbaceous matter, tend to have a higher and more stable combustion completeness. The inability of current static AGB products to capture these dynamic, biome-dependent variations in fuel availability and consumption is a fundamental limitation. While our use of NPP data for dynamic annual adjustment is an interim solution to capture some interannual variability, the advent of new-generation sensors fusing LiDAR, SAR, and passive microwave data promises to deliver high-resolution, dynamic AGB fields, which would fundamentally advance fuel load estimation (Cao et al., 2016; Liu et al., 2019; Rodríguez-Fernández et al., 2018). For the top-down path, the primary challenge is extrapolating full-day FRE from the snapshots provided by polar-orbiting satellites. Our Gaussian model for reconstructing the diurnal FRP cycle represents a significant improvement over simple linear methods. However, the true breakthrough will come from the direct integration of the FRP diurnal cycle using minute-level observations from new-generation geostationary satellites (e.g., FY-4, Himawari-8/9), which will eliminate the need for empirical models and greatly enhance the physical realism of FRE estimates. Finally, both pathways depend on EFs to convert energy release or biomass burned into pollutant emissions. Current static look-up tables fail to capture the vast EF variability within biomes or even across the lifecycle of a single fire (van Leeuwen et al., 2013; Yin, 2022). Future improvements lie in two areas. One is the development of more comprehensive EF libraries through advanced molecular-level speciation of aerosols (Jen et al., 2019; Koss et al., 2018), and the other is the creation of dynamic, high-resolution EF datasets by leveraging co-located trace gas measurements (e.g., CO/NO₂ ratios from TROPOMI) to monitor combustion characteristics like the flaming-to-smoldering ratio in near-real-time (van der Velde et al., 2021). Therefore, while the MBEI currently quantifies uncertainty by integrating



existing methods, its flexible architecture is explicitly designed to serve as a platform for incorporating these future data streams. This ensures a clear pathway for the iterative refinement of biomass burning inventories, moving the field toward more comprehensive and accurate assessments.

5 Conclusion

This study systematically assessed global biomass burning emissions and their uncertainties from 2003–2023 using the MBEI, an ensemble framework of eight sub-inventories that integrates both bottom-up and top-down approaches. A key finding is the spatial separation between the emission hotspots and the uncertainty hotspots. While high-emission regions in Africa and South America account for 64.4% of global CO₂ emissions, the structural uncertainty there is relatively constrained (max/min ratio < 2.0). In contrast, the greatest uncertainty (max/min ratio > 6.0) is found in lower-emission regions characterized by extreme, intermittent fires (e.g., AUST) or scattered agricultural burning (e.g., the MIDE).

Temporally, our analysis reveals a significant shift in the drivers of global biomass burning emissions over the past two decades. Although the overall long-term trend is not statistically significant, we identify a clear transition, the period dominated by declining tropical fire activity (2003–2013) was followed by a period increasingly influenced by intensifying high-latitude boreal fires and frequent climate-driven extreme events (2013–2023).

The spatial heterogeneity and temporal shift highlight the growing complexity of the global biomass burning emission regimes. The primary contribution of the MBEI framework is therefore its ability to explicitly quantify this structural uncertainty. It provides a central estimate consistent with the multi-inventory average, along with an uncertainty range that encompasses the estimates of major existing products. MBEI offers the crucial boundary conditions needed for Earth system models to estimate related environmental or exposure risk.

To effectively assess the complex dynamics of global biomass burning emission, the results of this study indicate that the focus should evolve from pursuing a single best estimate to embracing a probabilistic, uncertainty-aware approach. It is suggested that such data-constrained uncertainty information should be directly integrated into atmospheric chemistry and Earth system models. This is essential not only for improving model fidelity but also for conducting more robust risk assessments that consider plausible



688 high-end emission scenarios. Ultimately, the MBEI's explicit quantification of uncertainty provides a
689 more solid scientific foundation for developing resilient environmental and climate policies.

690

691 **Data availability.** The developed MBEI emission inventory described in this paper is available from
692 Zenodo: 10.5281/zenodo.17128279 (Liu and Yin, 2023). For further support or guidance regarding data
693 use, please contact yinshuai@aircas.ac.cn.

694 **Supplement.**

695 **Author contributions.** SY and ZS were responsible for the conceptualization of the study, project
696 administration, supervision, and funding acquisition. XL designed the methodology, developed the
697 software, performed the formal analysis and investigation, curated the data, prepared the visualizations
698 and wrote the original draft of the manuscript. CS contributed to the methodology development and
699 software implementation. TN, PW, QC and LS assisted with the formal analysis and data curation. HS,
700 DJ, MG, KY, ZT, LW, and XL contributed to the investigation, validation, and provision of resources.
701 All authors participated in the review and editing of the manuscript and have approved the final version
702 for publication.

703 **Competing interests.** The contact author has declared that none of the authors has any competing
704 interests.

705 **Disclaimer.** Publisher's note: Copernicus Publications remains neutral with regard to jurisdictional
706 claims in published maps and institutional affiliations. While Copernicus Publications makes every effort
707 to ensure appropriate place names are included, the final responsibility lies with the authors.

708 **Acknowledgements.** The authors would like to thank J. W. Kaiser for providing access to the most recent
709 data. We also acknowledge the support of the State Key Laboratory of Remote Sensing and Digital Earth,
710 Aerospace Information Research Institute, Chinese Academy of Sciences. The authors extend their
711 gratitude to the anonymous reviewers for their constructive comments, which greatly helped improve the
712 quality of this paper.

713 **Financial support.** This research is supported by the National Natural Science Foundation of China
714 (grant no. 42475142).



715 **Reference**

- 716 Andela, N., Kaiser, J. W., van der Werf, G. R., and Wooster, M. J.: New fire diurnal cycle
 717 characterizations to improve fire radiative energy assessments made from MODIS observations,
 718 Atmospheric Chemistry and Physics, 15, 8831–8846, <https://doi.org/10.5194/acp-15-8831-2015>, 2015.
- 719 Andela, N., Morton, D. C., Giglio, L., Chen, Y., van der Werf, G. R., Kasibhatla, P. S., DeFries, R. S.,
 720 Collatz, G. J., Hantson, S., Kloster, S., Bachelet, D., Forrest, M., Lasslop, G., Li, F., Mangeon, S., Melton,
 721 J. R., Yue, C., and Randerson, J. T.: A human-driven decline in global burned area, Science, 356, 1356–
 722 1362, <https://doi.org/10.1126/science.aal4108>, 2017.
- 723 Andreae, M. O. and Merlet, P.: Emission of trace gases and aerosols from biomass burning, Global
 724 Biogeochemical Cycles, 15, 955–966, <https://doi.org/10.1029/2000GB001382>, 2001.
- 725 Andreae, M. O.: Emission of trace gases and aerosols from biomass burning – an updated assessment,
 726 Atmospheric Chemistry and Physics, 19, 8523–8546, <https://doi.org/10.5194/acp-19-8523-2019>, 2019.
- 727 Binte Shahid, S., Lacey, F. G., Wiedinmyer, C., Yokelson, R. J., and Barsanti, K. C.: NEIVAv1.0: Next-
 728 generation emissions inventory expansion of Akagi et al. (2011) version 1.0, Geoscientific Model
 729 Development, 17, 7679–7711, <https://doi.org/10.5194/gmd-17-7679-2024>, 2024.
- 730 Bowman, D. M. J. S., Balch, J. K., Artaxo, P., Bond, W. J., Carlson, J. M., Cochrane, M. A., D’Antonio,
 731 C. M., DeFries, R. S., Doyle, J. C., Harrison, S. P., Johnston, F. H., Keeley, J. E., Krawchuk, M. A., Kull,
 732 C. A., Marston, J. B., Moritz, M. A., Prentice, I. C., Roos, C. I., Scott, A. C., Swetnam, T. W., van der
 733 Werf, G. R., and Pyne, S. J.: Fire in the earth system, Science, 324, 481–484,
 734 <https://doi.org/10.1126/science.1163886>, 2009.
- 735 Bray, C. D., Battye, W. H., Aneja, V. P., and Schlesinger, W. H.: Global emissions of NH₃, NO_x, and N₂O
 736 from biomass burning and the impact of climate change, Journal of the Air & Waste Management
 737 Association, 71, 102–114, <https://doi.org/10.1080/10962247.2020.1842822>, 2021.
- 738 Cao, L., Coops, N. C., Innes, J. L., Sheppard, S. R. J., Fu, L., Ruan, H., and She, G.: Estimation of forest
 739 biomass dynamics in subtropical forests using multi-temporal airborne LiDAR data, Remote Sensing of
 740 Environment, 178, 158–171, <https://doi.org/10.1016/j.rse.2016.03.012>, 2016.
- 741 Chen, Y., Morton, D. C., Andela, N., van der Werf, G. R., Giglio, L., and Randerson, J. T.: A pan-tropical
 742 cascade of fire driven by el niño/southern oscillation, Nature Climate Change, 7, 906–911,
 743 <https://doi.org/10.1038/s41558-017-0014-8>, 2017.



744 Cunningham, C. X., Williamson, G. J., and Bowman, D. M. J. S.: Increasing frequency and intensity of
 745 the most extreme wildfires on earth, *Nature Ecology & Evolution*, 8, 1420–1425,
 746 <https://doi.org/10.1038/s41559-024-02452-2>, 2024.

747 Filonchyk, M., Peterson, M. P., Zhang, L., Hurynovich, V., and He, Y.: Greenhouse gases emissions and
 748 global climate change: Examining the influence of CO₂, CH₄, and N₂O, *Science of The Total*
 749 *Environment*, 935, 173359, <https://doi.org/10.1016/j.scitotenv.2024.173359>, 2024.

750 Friedl, M. and Sulla-Menashe, D.: MODIS/terra+aqua land cover type yearly L3 global 500m SIN grid
 751 V061, NASA LP DAAC [data set], <https://doi.org/10.5067/MODIS/MCD12Q1.061>, 2022.

752 Friedlingstein, P., O’Sullivan, M., Jones, M. W., Andrew, R. M., Hauck, J., Landschützer, P., Le Quéré,
 753 C., Li, H., Luijkx, I. T., Olsen, A., Peters, G. P., Peters, W., Pongratz, J., Schwingshackl, C., Sitch, S.,
 754 Canadell, J. G., Ciais, P., Jackson, R. B., Alin, S. R., Arneeth, A., Arora, V., Bates, N. R., Becker, M.,
 755 Bellouin, N., Berghoff, C. F., Bittig, H. C., Bopp, L., Cadule, P., Campbell, K., Chamberlain, M. A.,
 756 Chandra, N., Chevallier, F., Chini, L. P., Colligan, T., Decayeux, J., Djeutchouang, L. M., Dou, X., Duran
 757 Rojas, C., Enyo, K., Evans, W., Fay, A. R., Feely, R. A., Ford, D. J., Foster, A., Gasser, T., Gehlen, M.,
 758 Gkritzalis, T., Grassi, G., Gregor, L., Gruber, N., Gürses, Ö., Harris, I., Hefner, M., Heinke, J., Hurtt, G.
 759 C., Iida, Y., Ilyina, T., Jacobson, A. R., Jain, A. K., Jarníková, T., Jersild, A., Jiang, F., Jin, Z., Kato, E.,
 760 Keeling, R. F., Klein Goldewijk, K., Knauer, J., Korsbakken, J. I., Lan, X., Lauvset, S. K., Lefèvre, N.,
 761 Liu, Z., Liu, J., Ma, L., Maksyutov, S., Marland, G., Mayot, N., McGuire, P. C., Metzl, N., Monacchi, N.
 762 M., Morgan, E. J., Nakaoka, S.-I., Neill, C., Niwa, Y., Nützel, T., Olivier, L., Ono, T., Palmer, P. I., Pierrot,
 763 D., Qin, Z., Resplandy, L., Roobaert, A., Rosan, T. M., Rödenbeck, C., Schwinger, J., Smallman, T. L.,
 764 Smith, S. M., Sospedra-Alfonso, R., Steinhoff, T., Sun, Q., Sutton, A. J., Séférian, R., Takao, S., Tatebe,
 765 H., Tian, H., Tilbrook, B., Torres, O., Tourigny, E., Tsujino, H., Tubiello, F., van der Werf, G.,
 766 Wanninkhof, R., Wang, X., Yang, D., Yang, X., Yu, Z., Yuan, W., Yue, X., Zaehle, S., Zeng, N., and Zeng,
 767 J.: Global carbon budget 2024, *Earth System Science Data*, 17, 965–1039, [https://doi.org/10.5194/essd-](https://doi.org/10.5194/essd-17-965-2025)
 768 [17-965-2025](https://doi.org/10.5194/essd-17-965-2025), 2025.

769 Giglio, L., Schroeder, W., and Hall, J. V.: MODIS collection 6 active fire product user’s guide revision
 770 C, NASA, available at: [https://modis-](https://modis-fire.umd.edu/files/MODIS_C6_C6.1_Active_Fire_User_Guide_C.pdf)
 771 [fire.umd.edu/files/MODIS_C6_C6.1_Active_Fire_User_Guide_C.pdf](https://modis-fire.umd.edu/files/MODIS_C6_C6.1_Active_Fire_User_Guide_C.pdf) (last access: 15 August 2025),
 772 2020.



- 773 Giglio, L., van der Werf, G. R., Randerson, J. T., Collatz, G. J., and Kasibhatla, P.: Global estimation of
 774 burned area using MODIS active fire observations, *Atmospheric Chemistry and Physics*, 6, 957–974,
 775 <https://doi.org/10.5194/acp-6-957-2006>, 2006.
- 776 Hoelzemann, J. J., Schultz, M. G., Brasseur, G. P., Granier, C., and Simon, M.: Global wildland fire
 777 emission model (GWEM): Evaluating the use of global area burnt satellite data, *Journal of Geophysical*
 778 *Research: Atmospheres*, 109, <https://doi.org/10.1029/2003JD003666>, 2004.
- 779 Ichoku, C. and Ellison, L.: Global top-down smoke-aerosol emissions estimation using satellite fire
 780 radiative power measurements, *Atmospheric Chemistry and Physics*, 14, 6643–6667,
 781 <https://doi.org/10.5194/acp-14-6643-2014>, 2014.
- 782 Ichoku, C. and Kaufman, Y. J.: A method to derive smoke emission rates from MODIS fire radiative
 783 energy measurements, *IEEE Transactions on Geoscience and Remote Sensing*, 43, 2636–2649,
 784 <https://doi.org/10.1109/TGRS.2005.857328>, 2005.
- 785 Ito, A. and Penner, J. E.: Global estimates of biomass burning emissions based on satellite imagery for
 786 the year 2000, *Journal of Geophysical Research: Atmospheres*, 109,
 787 <https://doi.org/10.1029/2003JD004423>, 2004.
- 788 Jain, P., Barber, Q. E., Taylor, S. W., Whitman, E., Castellanos Acuna, D., Boulanger, Y., Chavardès, R.
 789 D., Chen, J., Englefield, P., Flannigan, M., Girardin, M. P., Hanes, C. C., Little, J., Morrison, K., Skakun,
 790 R. S., Thompson, D. K., Wang, X., and Parisien, M.-A.: Drivers and impacts of the record-breaking 2023
 791 wildfire season in Canada, *Nature Communications*, 15, 6764, [https://doi.org/10.1038/s41467-024-](https://doi.org/10.1038/s41467-024-51154-7)
 792 [51154-7](https://doi.org/10.1038/s41467-024-51154-7), 2024.
- 793 Jen, C. N., Hatch, L. E., Selimovic, V., Yokelson, R. J., Weber, R., Fernandez, A. E., Kreisberg, N. M.,
 794 Barsanti, K. C., and Goldstein, A. H.: Speciated and total emission factors of particulate organics from
 795 burning western US wildland fuels and their dependence on combustion efficiency, *Atmospheric*
 796 *Chemistry and Physics*, 19, 1013–1026, <https://doi.org/10.5194/acp-19-1013-2019>, 2019.
- 797 Jones, M. W., Abatzoglou, J. T., Veraverbeke, S., Andela, N., Lasslop, G., Forkel, M., Smith, A. J. P.,
 798 Burton, C., Betts, R. A., van der Werf, G. R., Sitch, S., Canadell, J. G., Santín, C., Kolden, C., Doerr, S.
 799 H., and Le Quéré, C.: Global and regional trends and drivers of fire under climate change, *Reviews of*
 800 *Geophysics*, 60, e2020RG000726, <https://doi.org/10.1029/2020RG000726>, 2022.
- 801 Kaiser, J. W., Heil, A., Andreae, M. O., Benedetti, A., Chubarova, N., Jones, L., Morcrette, J.-J., Razinger,
 802 M., Schultz, M. G., Suttie, M., and van der Werf, G. R.: Biomass burning emissions estimated with a



803 global fire assimilation system based on observed fire radiative power, *Biogeosciences*, 9, 527–554,
 804 <https://doi.org/10.5194/bg-9-527-2012>, 2012.

805 Kaiser, J. W., Holmedal, D. G., Ytre-Eide, M. A., and de Jong, M.: GFAS4HTAP vegetation fire
 806 emissions 2003–2023, Zenodo [data set], <https://doi.org/10.5281/zenodo.15721463>, 2023.

807 Koss, A. R., Sekimoto, K., Gilman, J. B., Selimovic, V., Coggon, M. M., Zarzana, K. J., Yuan, B., Lerner,
 808 B. M., Brown, S. S., Jimenez, J. L., Krechmer, J., Roberts, J. M., Warneke, C., Yokelson, R. J., and de
 809 Gouw, J.: Non-methane organic gas emissions from biomass burning: Identification, quantification, and
 810 emission factors from PTR-ToF during the FIREX 2016 laboratory experiment, *Atmospheric Chemistry*
 811 *and Physics*, 18, 3299–3319, <https://doi.org/10.5194/acp-18-3299-2018>, 2018.

812 Koster, R. D., Darmenov, A. S., and da Silva, A. M.: The quick fire emissions dataset (QFED):
 813 Documentation of versions 2.1, 2.2 and 2.4: technical report series on global modeling and data
 814 assimilation - volume 38, NASA, available at: <https://ntrs.nasa.gov/citations/20180005253> (last access:
 815 15 August 2025), 2015.

816 Letu, H., Ma, R., Nakajima, T. Y., Shi, C., Hashimoto, M., Nagao, T. M., Baran, A. J., Nakajima, T., Xu,
 817 J., Wang, T., Tana, G., Bilige, S., Shang, H., Chen, L., Ji, D., Lei, Y., Wei, L., Zhang, P., Li, J., Li, L.,
 818 Zheng, Y., Khatri, P., and Shi, J.: Surface solar radiation compositions observed from himawari-8/9 and
 819 fengyun-4 series, *Bulletin of the American Meteorological Society*, 104, E1839–E1856,
 820 <https://doi.org/10.1175/BAMS-D-22-0154.1>, 2023.

821 Li, K., Zheng, F., Cheng, L., Zhang, T., and Zhu, J.: Record-breaking global temperature and crises with
 822 strong El Niño in 2023–2024, *The Innovation Geoscience*, 1, 100030, doi:10.59717/j.xinn-
 823 geo.2023.100030, 2023.

824 Liu, T., Mickley, L. J., Marlier, M. E., DeFries, R. S., Khan, M. F., Latif, M. T., and Karambelas, A.:
 825 Diagnosing spatial biases and uncertainties in global fire emissions inventories: Indonesia as regional
 826 case study, *Remote Sensing of Environment*, 237, 111557, <https://doi.org/10.1016/j.rse.2019.111557>,
 827 2020.

828 Liu, X. and Yin, S.: Multi-ensemble Biomass-burning Emissions Inventory (MBEI)_v1.1, Zenodo [data
 829 set], <https://doi.org/10.5281/zenodo.17128279>, 2023.

830 Liu, Y., Chen, J., Shi, Y., Zheng, W., Shan, T., and Wang, G.: Global emissions inventory from open
 831 biomass burning (GEIOBB): Utilizing fengyun-3D global fire spot monitoring data, *Earth System*
 832 *Science Data*, 16, 3495–3515, <https://doi.org/10.5194/essd-16-3495-2024>, 2024.



833 Liu, Y., Gong, W., Xing, Y., Hu, X., and Gong, J.: Estimation of the forest stand mean height and
 834 aboveground biomass in northeast China using SAR sentinel-1B, multispectral sentinel-2A, and DEM
 835 imagery, *ISPRS Journal of Photogrammetry and Remote Sensing*, 151, 277–289,
 836 <https://doi.org/10.1016/j.isprsjprs.2019.03.016>, 2019.

837 Longo, K. M., Freitas, S. R., Andreae, M. O., Setzer, A., Prins, E., and Artaxo, P.: The coupled aerosol
 838 and tracer transport model to the brazilian developments on the regional atmospheric modeling system
 839 (CATT-BRAMS) – part 2: Model sensitivity to the biomass burning inventories, *Atmospheric Chemistry*
 840 *and Physics*, 10, 5785–5795, <https://doi.org/10.5194/acp-10-5785-2010>, 2010.

841 Luo, B., Xiao, C., Luo, D., Fu, Q., Chen, D., Zhang, Q., Ge, Y., and Diao, Y.: Atmospheric and oceanic
 842 drivers behind the 2023 canadian wildfires, *Communications Earth & Environment*, 6, 446,
 843 <https://doi.org/10.1038/s43247-025-02387-x>, 2025.

844 Mann, H. B.: Nonparametric tests against trend, *Econometrica*, 13, 245–259,
 845 <https://doi.org/10.2307/1907187>, 1945.

846 Mariani, M., Fletcher, M.-S., Holz, A., and Nyman, P.: ENSO controls interannual fire activity in
 847 southeast australia, *Geophysical Research Letters*, 43, 10891–10900,
 848 <https://doi.org/10.1002/2016GL070572>, 2016.

849 Matthias, V., Arndt, Jan A., Aulinger, Armin, Bieser, Johannes, Denier van der Gon, Hugo, Kranenburg,
 850 Richard, Kuenen, Jeroen, Neumann, Daniel, Pouliot, George, and Quante, M.: Modeling emissions for
 851 three-dimensional atmospheric chemistry transport models, *Journal of the Air & Waste Management*
 852 *Association*, 68, 763–800, <https://doi.org/10.1080/10962247.2018.1424057>, 2018.

853 Mieville, A., Granier, C., Liousse, C., Guillaume, B., Mouillot, F., Lamarque, J.-F., Grégoire, J.-M., and
 854 Pétron, G.: Emissions of gases and particles from biomass burning during the 20th century using satellite
 855 data and an historical reconstruction, *Atmospheric Environment*, 44, 1469–1477,
 856 <https://doi.org/10.1016/j.atmosenv.2010.01.011>, 2010.

857 N'Datchoh, T. E., Liousse, C., Roblou, L., and N'Dri, A. B.: Biomass burning over africa: How to explain
 858 the differences observed between the different emission inventories?, *Atmosphere*, 16, 440,
 859 <https://doi.org/10.3390/atmos16040440>, 2025.

860 NASA VIIRS Land Science Team: VIIRS (NOAA-21/JPSS-2) I band 375 m active fire product NRT
 861 (vector data), NASA FIRMS [data set], <https://doi.org/10.5067/FIRMS/MODIS/MCD14DL.NRT.0061>,
 862 2021.



- 863 Pan, X., Ichoku, C., Chin, M., Bian, H., Darmenov, A., Colarco, P., Ellison, L., Kucsera, T., da Silva, A.,
 864 Wang, J., Oda, T., and Cui, G.: Six global biomass burning emission datasets: Intercomparison and
 865 application in one global aerosol model, *Atmospheric Chemistry and Physics*, 20, 969–994,
 866 <https://doi.org/10.5194/acp-20-969-2020>, 2020.
- 867 Pellegrini, A. F. A., Ahlström, A., Hobbie, S. E., Reich, P. B., Nieradzik, L. P., Staver, A. C., Scharenbroch,
 868 B. C., Jumpponen, A., Anderegg, W. R. L., Randerson, J. T., and Jackson, R. B.: Fire frequency drives
 869 decadal changes in soil carbon and nitrogen and ecosystem productivity, *Nature*, 553, 194–198,
 870 <https://doi.org/10.1038/nature24668>, 2018.
- 871 Pereira, G., Siqueira, R., Rosário, N. E., Longo, K. L., Freitas, S. R., Cardozo, F. S., Kaiser, J. W., and
 872 Wooster, M. J.: Assessment of fire emission inventories during the south American biomass burning
 873 analysis (SAMBBA) experiment, *Atmospheric Chemistry and Physics*, 16, 6961–6975,
 874 <https://doi.org/10.5194/acp-16-6961-2016>, 2016.
- 875 Raich, J. W., Russell, A. E., Kitayama, K., Parton, W. J., and Vitousek, P. M.: Temperature influences
 876 carbon accumulation in moist tropical forests, *Ecology*, 87, 76–87, <https://doi.org/10.1890/05-0023>, 2006.
- 877 Ramanathan, V. and Carmichael, G.: Global and regional climate changes due to black carbon, *Nature*
 878 *Geoscience*, 1, 221–227, <https://doi.org/10.1038/ngeo156>, 2008.
- 879 Reid, J. S., Koppmann, R., Eck, T. F., and Eleuterio, D. P.: A review of biomass burning emissions part
 880 II: Intensive physical properties of biomass burning particles, *Atmospheric Chemistry and Physics*, 5,
 881 799–825, <https://doi.org/10.5194/acp-5-799-2005>, 2005.
- 882 Rodríguez-Fernández, N. J., Mialon, A., Mermoz, S., Bouvet, A., Richaume, P., Al Bitar, A., Al-Yaari,
 883 A., Brandt, M., Kaminski, T., Le Toan, T., Kerr, Y. H., and Wigneron, J.-P.: An evaluation of SMOS L-
 884 band vegetation optical depth (L-VOD) data sets: High sensitivity of L-VOD to above-ground biomass
 885 in africa, *Biogeosciences*, 15, 4627–4645, <https://doi.org/10.5194/bg-15-4627-2018>, 2018.
- 886 Running, S. and Zhao, M.: MODIS/aqua net primary production gap-filled yearly L4 global 500m SIN
 887 grid V061, NASA Land Processes Distributed Active Archive Center (LP DAAC) [data set],
 888 <https://doi.org/10.5067/MODIS/MYD17A3HGF.061>, 2021.
- 889 Santoro, M. and Cartus, O.: ESA biomass climate change initiative (biomass_cci): Global datasets of
 890 forest above-ground biomass for the years 2010, 2015, 2016, 2017, 2018, 2019, 2020 and 2021, v5.01
 891 (5.01), Centre for Environmental Data Analysis (CEDA) [data set],
 892 <https://doi.org/10.5285/bf535053562141c6bb7ad831f5998d77>, 2024.



- 893 Santoro, M.: GlobBiomass - global datasets of forest biomass, PANGAEA [data set],
 894 <https://doi.org/10.1594/PANGAEA.894711>, 2018.
- 895 Seiler, W. and Crutzen, P. J.: Estimates of gross and net fluxes of carbon between the biosphere and the
 896 atmosphere from biomass burning, *Climatic Change*, 2, 207–247, <https://doi.org/10.1007/BF00137988>,
 897 1980.
- 898 Sen, P. K.: Estimates of the regression coefficient based on kendall's tau, *Journal of the American*
 899 *Statistical Association*, 63, 1379–1389, <https://doi.org/10.1080/01621459.1968.10480934>, 1968.
- 900 Senande-Rivera, M., Insua-Costa, D., and Miguez-Macho, G.: Spatial and temporal expansion of global
 901 wildland fire activity in response to climate change, *Nature Communications*, 13, 1208,
 902 <https://doi.org/10.1038/s41467-022-28835-2>, 2022.
- 903 Shi, C., Letu, H., et al.: Near-global monitoring of surface solar radiation through the construction of a
 904 geostationary satellite network observation system, *The Innovation*, 6, 100876,
 905 <https://doi.org/10.1016/j.xinn.2025.100876>, 2025.
- 906 Shi, Y. and Matsunaga, T.: Temporal comparison of global inventories of CO₂ emissions from biomass
 907 burning during 2002–2011 derived from remotely sensed data, *Environmental Science and Pollution*
 908 *Research*, 24, 16905–16916, <https://doi.org/10.1007/s11356-017-9141-z>, 2017.
- 909 Shi, Y., Matsunaga, T., Saito, M., Yamaguchi, Y., and Chen, X.: Comparison of global inventories of CO₂
 910 emissions from biomass burning during 2002–2011 derived from multiple satellite products,
 911 *Environmental Pollution*, 206, 479–487, <https://doi.org/10.1016/j.envpol.2015.08.009>, 2015.
- 912 Silva, S. S. da, Fearnside, P. M., Graça, P. M. L. de A., Brown, I. F., Alencar, A., and Melo, A. W. F. de:
 913 Dynamics of forest fires in the southwestern amazon, *Forest Ecology and Management*, 424, 312–322,
 914 <https://doi.org/10.1016/j.foreco.2018.04.041>, 2018.
- 915 Stroppiana, D., Brivio, P. A., Grégoire, J.-M., Liousse, C., Guillaume, B., Granier, C., Mieville, A., Chin,
 916 M., and Pétron, G.: Comparison of global inventories of CO emissions from biomass burning derived
 917 from remotely sensed data, *Atmospheric Chemistry and Physics*, 10, 12173–12189,
 918 <https://doi.org/10.5194/acp-10-12173-2010>, 2010.
- 919 Su, M., Shi, Y., Yang, Y., and Guo, W.: Impacts of different biomass burning emission inventories:
 920 Simulations of atmospheric CO₂ concentrations based on GEOS-chem, *Science of The Total*
 921 *Environment*, 876, 162825, <https://doi.org/10.1016/j.scitotenv.2023.162825>, 2023.



922 Touma, D., Stevenson, S., Lehner, F., and Coats, S.: Human-driven greenhouse gas and aerosol emissions
 923 cause distinct regional impacts on extreme fire weather, *Nature Communications*, 12, 212,
 924 <https://doi.org/10.1038/s41467-020-20570-w>, 2021.

925 Tyukavina, A., Potapov, P., Hansen, M. C., et al.: Global trends of forest loss due to fire from 2001 to
 926 2019, *Frontiers in Remote Sensing*, 3, 825190, <https://doi.org/10.3389/frsen.2022.825190>, 2022.

927 van der Velde, I. R., van der Werf, G. R., Houweling, S., Eskes, H. J., Veeffkind, J. P., Borsdorff, T., and
 928 Aben, I.: Biomass burning combustion efficiency observed from space using measurements of CO and
 929 NO₂ by the TROPOspheric monitoring instrument (TROPOMI), *Atmospheric Chemistry and Physics*,
 930 21, 597–616, <https://doi.org/10.5194/acp-21-597-2021>, 2021.

931 van der Werf, G. R., Morton, D. C., DeFries, R. S., Giglio, L., Randerson, J. T., Collatz, G. J., and
 932 Kasibhatla, P. S.: Estimates of fire emissions from an active deforestation region in the southern amazon
 933 based on satellite data and biogeochemical modelling, *Biogeosciences*, 6, 235–249,
 934 <https://doi.org/10.5194/bg-6-235-2009>, 2009.

935 van der Werf, G. R., Randerson, J. T., Giglio, L., Collatz, G. J., Kasibhatla, P. S., and Arellano, A. F. J.:
 936 Interannual variability in global biomass burning emissions from 1997 to 2004, *Atmospheric Chemistry*
 937 *and Physics*, 6, 3423–3441, <https://doi.org/10.5194/acp-6-3423-2006>, 2006.

938 van der Werf, G. R., Randerson, J. T., Giglio, L., van Leeuwen, T. T., Chen, Y., Rogers, B. M., Mu, M.,
 939 van Marle, M. J. E., Morton, D. C., Collatz, G. J., Yokelson, R. J., and Kasibhatla, P. S.: Global fire
 940 emissions estimates during 1997–2016, *Earth System Science Data*, 9, 697–720,
 941 <https://doi.org/10.5194/essd-9-697-2017>, 2017.

942 van Leeuwen, T. T., Peters, W., Krol, M. C., and van der Werf, G. R.: Dynamic biomass burning emission
 943 factors and their impact on atmospheric CO mixing ratios, *Journal of Geophysical Research:*
 944 *Atmospheres*, 118, 6797–6815, <https://doi.org/10.1002/jgrd.50478>, 2013.

945 van Wees, D., van der Werf, G. R., Randerson, J. T., Andela, N., Chen, Y., and Morton, D. C.: The role
 946 of fire in global forest loss dynamics, *Global Change Biology*, 27, 2377–2391,
 947 <https://doi.org/10.1111/gcb.15591>, 2021.

948 Vermote, E., Ellicott, E., Dubovik, O., Lapyonok, T., Chin, M., Giglio, L., and Roberts, G. J.: An
 949 approach to estimate global biomass burning emissions of organic and black carbon from MODIS fire
 950 radiative power, *Journal of Geophysical Research: Atmospheres*, 114, D18205,
 951 <https://doi.org/10.1029/2008JD011188>, 2009.



952 Vernooij, R., Eames, T., Russell-Smith, J., Yates, C., Beatty, R., Evans, J., Edwards, A., Ribeiro, N.,
 953 Wooster, M., Strydom, T., Giongo, M. V., Borges, M. A., Menezes Costa, M., Barradas, A. C. S., van
 954 Wees, D., and Van der Werf, G. R.: Dynamic savanna burning emission factors based on satellite data
 955 using a machine learning approach, *Earth System Dynamics*, 14, 1039–1064,
 956 <https://doi.org/10.5194/esd-14-1039-2023>, 2023.

957 Wang, F., Harindintwali, J. D., Wei, K., Shan, Y., Mi, Z., Costello, M. J., Grunwald, S., Feng, Z., Wang,
 958 F., Guo, Y., Wu, X., Kumar, P., Kästner, M., Feng, X., Kang, S., Liu, Z., Fu, Y., Zhao, W., Ouyang, C.,
 959 Shen, J., Wang, H., Chang, S. X., Evans, D. L., Wang, R., Zhu, C., Xiang, L., Rinklebe, J., Du, M., Huang,
 960 L., Bai, Z., Li, S., Lal, R., Elsner, M., Wigner, J.-P., Florindo, F., Jiang, X., Shaheen, S. M., Zhong, X.,
 961 Bol, R., Vasques, G. M., Li, X., Pfautsch, S., Wang, M., He, X., Agathokleous, E., Du, H., Yan, H.,
 962 Kengara, F. O., Brahushi, F., Long, X.-E., Pereira, P., Ok, Y. S., Rillig, M. C., Jeppesen, E., Barceló, D.,
 963 Yan, X., Jiao, N., Han, B., Schäffer, A., Chen, J. M., Zhu, Y., Cheng, H., Amelung, W., Spötl, C., Zhu, J.,
 964 and Tiedje, J. M.: Climate change: strategies for mitigation and adaptation, *The Innovation Geoscience*,
 965 1, 100015, doi:10.59717/j.xinn-geo.2023.100015, 2023.

966 Whitburn, S., Damme, M. V., Clarisse, L., Turquety, S., Clerbaux, C., and Coheur, P.-F.: Doubling of
 967 annual ammonia emissions from the peat fires in indonesia during the 2015 el niño, *Geophysical*
 968 *Research Letters*, 43, 11007–11014, <https://doi.org/10.1002/2016GL070620>, 2016.

969 Whittaker, R. H. and Likens, G. E.: Carbon in the biota, in: *Carbon and the Biosphere*, edited by:
 970 Woodwell, G. M. and Pecan, E. V., U.S. Atomic Energy Commission, Washington, D.C., 281–302, 1972.

971 Wiedinmyer, C., Kimura, Y., McDonald-Buller, E. C., Emmons, L. K., Buchholz, R. R., Tang, W., Seto,
 972 K., Joseph, M. B., Barsanti, K. C., Carlton, A. G., and Yokelson, R.: The fire inventory from NCAR
 973 version 2.5: An updated global fire emissions model for climate and chemistry applications, *Geoscientific*
 974 *Model Development*, 16, 3873–3891, <https://doi.org/10.5194/gmd-16-3873-2023>, 2023.

975 Wiedinmyer, C., Quayle, B., Geron, C., Belote, A., McKenzie, D., Zhang, X., O'Neill, S., and Wynne,
 976 K. K.: Estimating emissions from fires in north America for air quality modeling, *Atmospheric*
 977 *Environment*, 40, 3419–3432, <https://doi.org/10.1016/j.atmosenv.2006.02.010>, 2006.

978 Wiggins, E. B., Andrews, A., Sweeney, C., Miller, J. B., Miller, C. E., Veraverbeke, S., Commene, R.,
 979 Wofsy, S., Henderson, J. M., and Randerson, J. T.: Boreal forest fire CO and CH₄ emission factors derived
 980 from tower observations in alaska during the extreme fire season of 2015, *Atmospheric Chemistry and*
 981 *Physics*, 21, 8557–8574, <https://doi.org/10.5194/acp-21-8557-2021>, 2021.



Williams, J. E., Weele, M. van, Velthoven, P. F. J. van, Scheele, M. P., Liousse, C., and Werf, G. R. van
 der: The impact of uncertainties in african biomass burning emission estimates on modeling global air
 quality, long range transport and tropospheric chemical lifetimes, *Atmosphere*, 3, 132–163,
<https://doi.org/10.3390/atmos3010132>, 2012.

Wooster, M. J., Roberts, G., Perry, G. L. W., and Kaufman, Y. J.: Retrieval of biomass combustion rates
 and totals from fire radiative power observations: FRP derivation and calibration relationships between
 biomass consumption and fire radiative energy release, *Journal of Geophysical Research: Atmospheres*,
 110, D24310, <https://doi.org/10.1029/2005JD006318>, 2005.

Yin, S.: Decadal trends of MERRA-estimated PM_{2.5} concentrations in East Asia and potential exposure
 from 1990 to 2019, *Atmospheric Environment*, 264, 118690, doi:10.1016/j.atmosenv.2021.118690, 2021.

Yin, S., Shi, C., Letu, H., Ito, A., Shang, H., Ji, D., Li, L., Bilige, S., Nie, T., Yi, K., Guo, M., Sun, Z.,
 and Li, A.: Reconstruction of PM_{2.5} concentrations in east asia on the basis of a wide-deep ensemble
 machine learning framework and estimation of the potential exposure level from 1981 to 2020,
Engineering, 49, 225–237, <https://doi.org/10.1016/j.eng.2024.09.025>, 2025.

Yin, S., Wang, X., Guo, M., Santoso, H., and Guan, H.: The abnormal change of air quality and air
 pollutants induced by the forest fire in sumatra and borneo in 2015, *Atmospheric Research*, 243, 105027,
<https://doi.org/10.1016/j.atmosres.2020.105027>, 2020a.

Yin, S.: Effect of biomass burning on premature mortality associated with long-term exposure to PM_{2.5}
 in Equatorial Asia, *Journal of Environmental Management*, 330, 117154,
<https://doi.org/10.1016/j.jenvman.2022.117154>, 2023.

Yin, S.: Exploring the relationships between ground-measured particulate matter and satellite-retrieved
 aerosol parameters in China, *Environmental Science and Pollution Research*, 29, 44348–44363,
 doi:10.1007/s11356-022-19049-6, 2022.

Yin, Y., Bloom, A. A., Worden, J., Saatchi, S., Yang, Y., Williams, M., Liu, J., Jiang, Z., Worden, H.,
 Bowman, K., Frankenberg, C., and Schimel, D.: Fire decline in dry tropical ecosystems enhances decadal
 land carbon sink, *Nature Communications*, 11, 1900, <https://doi.org/10.1038/s41467-020-15852-2>,
 2020b.

Zhang, F., Wang, J., Ichoku, C., Hyer, E. J., Yang, Z., Ge, C., Su, S., Zhang, X., Kondragunta, S., and
 Kaiser, J. W.: Sensitivity of mesoscale modeling of smoke direct radiative effect to the emission inventory:



- 1011 A case study in northern sub-saharan african region, *Environmental Research Letters*, 9, 075002,
1012 <https://doi.org/10.1088/1748-9326/9/7/075002>, 2014.
- 1013 Zhang, Y., Albinet, A., Petit, J.-E., Jacob, V., Chevrier, F., Gille, G., Pontet, S., Chrétien, E., Dominik-
1014 Sègue, M., Levigoureux, G., Močnik, G., Gros, V., Jaffrezo, J.-L., and Favez, O.: Substantial brown
1015 carbon emissions from wintertime residential wood burning over france, *Science of The Total*
1016 *Environment*, 743, 140752, <https://doi.org/10.1016/j.scitotenv.2020.140752>, 2020.
- 1017 Zheng, B., Ciais, P., Chevallier, F., Chuvieco, E., Chen, Y., and Yang, H.: Increasing forest fire emissions
1018 despite the decline in global burned area, *Science Advances*, 7, eabh2646,
1019 <https://doi.org/10.1126/sciadv.abh2646>, 2021.
- 1020 Zheng, B., Ciais, P., Chevallier, F., Yang, H., Canadell, J. G., Chen, Y., van der Velde, I. R., Aben, I.,
1021 Chuvieco, E., Davis, S. J., Deeter, M., Hong, C., Kong, Y., Li, H., Li, H., Lin, X., He, K., and Zhang, Q.:
1022 Record-high CO₂ emissions from boreal fires in 2021, *Science*, 379, 912–917,
1023 <https://doi.org/10.1126/science.ade0805>, 2023.